Wnt-associated adult stem cell marker Lgr6 is required for osteogenesis and fracture healing

Laura Doherty[1,2,*], **Matthew Wan**[1,*], **Anna Peterson**[1], **Daniel W. Youngstrom**[1], **Justin S. King**[1], **Ivo Kalajzic**[2,3], **Kurt D. Hankenson**[4], **Archana Sanjay**[1]

[1]Department of Orthopaedic Surgery, UConn Musculoskeletal Institute, School of Medicine, UConn Health, Farmington, CT, 06030

[2]School of Dental Medicine, UConn Health, Farmington, CT, 06030

[3]Department of Reconstructive Sciences, School of Dental Medicine, UConn Health, Farmington, CT, 06030

[4]Department of Orthopaedic Surgery, School of Medicine, University of Michigan, Ann Arbor, MI, 48109

Abstract

Despite the remarkable regenerative capacity of skeletal tissues, nonunion of bone and failure of fractures to heal properly presents a significant clinical concern. Stem and progenitor cells are present in bone and become activated following injury; thus, elucidating mechanisms that promote adult stem cell-mediated healing is important. Wnt-associated adult stem marker Lgr6 is implicated in the regeneration of tissues with well-defined stem cell niches in stem cell-reliant organs. Here, we demonstrate that Lgr6 is dynamically expressed in osteoprogenitors in response to fracture injury. We used an *Lgr6*-null mouse model and found that *Lgr6* expression is necessary for maintaining bone volume and efficient postnatal bone regeneration in adult mice. Skeletal progenitors isolated from *Lgr6-null* mice have reduced colony-forming potential and reduced osteogenic differentiation capacity due to attenuated cWnt signaling. *Lgr6*-null mice consist of a lower proportion of self-renewing stem cells. In response to fracture injury, *Lgr6-null* mice have a deficiency in the proliferation of periosteal progenitors and reduced ALP activity. Further, analysis of the bone regeneration phase and remodeling phase of fracture healing in *Lgr6*-null mice showed impaired endochondral ossification and decreased mineralization. We propose that in contrast to

Corresponding Author: Archana Sanjay, Department of Orthopaedic Surgery, UConn Musculoskeletal Institute, UConn Health, 263 Farmington Ave, Farmington, CT, USA. 06030 860-679-4649, asanjay@uchc.edu.
*These authors have contributed equally.

Conflict of interests

The authors report no conflict of interest

not being required for successful skeletal development, Lgr6-positive cells have a direct role in endochondral bone repair.

Keywords

Fracture healing; bone regeneration; skeletal stem cells; periosteum; Lgr family

Introduction

Insufficient bone healing occurs with high incidence and remains a significant public health concern [1]. Common comorbidities and risk factors, including advanced age, diabetes, smoking, and inflammatory conditions, exacerbate bone healing abnormalities. In addition, fracture nonunion often requires additional surgical intervention, as there are limited therapeutic options at this stage of repair [2–4]. The consequence of delayed and failed fracture healing result in an enormous burden to the healthcare system[1]; therefore, efforts to improve approaches to enhance progenitor-mediated repair are increasingly necessary to advance the fields of orthopedics and regenerative medicine.

Skeletal regeneration leading to scarless tissue formation in adulthood is a complex process that involves the recruitment of progenitor cells from multiple sources. It is orchestrated via various signaling pathway interactions [5–7]. Following a fracture insult, stem and progenitor cells from the periosteum, bone marrow, and various other sources proliferate at the injury site [8–10]. In this endochondral ossification healing process, these cells differentiate into chondrocytes and osteoblasts to produce a cartilaginous matrix and osteoid, respectively; the generated fracture callus later becomes mineralized and is remodeled to its original architecture. The periosteal layer harbors essential osteochondral progenitors that are robustly activated following the fracture, contributing to the callus formation via endochondral ossification at the central injury area and intramembranous ossification flanking the fracture site [5,8–11]. Removal of the periosteum and the osteochondral progenitors within severely impair efficient fracture healing [5,8,10–12].

Leucine-rich repeat-containing G protein-coupled receptor 6 (Lgr6) is a protein in the G-protein-coupled 7-transmembrane superfamily [13]. Members of the Lgr family (Lgr4/5/6) are primarily characterized as adult stem cell markers that play a critical role in defining stem and progenitor cell behavior in established stem cell niches [14–16]. In adult stem cell-reliant organs (e.g., intestine, hair follicle, skin), different Lgrs mark distinct stem cell populations regarding location and function [14,15]. In some Wnt-driven stem cell compartments, Lgrs can serve an additional function as receptors in the Wnt/β-catenin pathway [17,18]; in this context, binding of soluble R-spondins (Rspo1-4) to Lgrs prolongs the presence of Frizzled (Fzd) receptors on the cell surface, as Lgrs interact with components of the Wnt signalosome. Recent work has also indicated that Lgr6 is dynamically expressed in mouse and human-derived mesenchymal stem cells and plays a role in osteogenesis [19–23]. However, very little is known about its role in bone regeneration, prompting our current studies on this gene in osteoblast differentiation and bone healing.

Here, we report that Lgr6 is dynamically expressed in osteoprogenitors in response to fracture injury. We found that ablation of Lgr6 reduces the bone volume in mature mice of either sex. Lgr6 is required for osteogenic differentiation *in vitro*, and its expression confers colony-forming potential in isolated mesenchymal progenitors from adult mice. Additionally, endochondral fracture healing and callus mineralization are significantly impaired in *Lgr6*-null mice. We propose that Lgr6-positive cells have a direct role in endochondral bone repair and that Lgr6 functions during postnatal bone regeneration, in contrast to not being required for successful skeletal development.

Results

Increased Lgr6 expression in a mouse model with enhanced periosteal response to injury

PI3K is a critical regulator of the major growth factors involved in fracture healing that promotes the proliferation, migration, and differentiation of osteoprogenitors[24,25]. The PI3K enzyme is a heterodimer of p110 catalytic and p85 regulatory subunits where p85 binds and stabilizes the p110 subunit [26,27]. We reported that an E3 ligase and adaptor protein Cbl binds to the p85 subunit and regulates PI3K activity[28–32]. We discovered that a point mutation in Cbl (Cbl^{Y737F}) disrupts the Cbl-p85 interaction but does not impact E3 ligase function or protein levels of Cbl and p85[33,34] We used a mouse model that harbors Cbl^{Y737} knock-in mutation ($gCbl^{YF}$)[35] to study the impact of PI3K signaling in bone modeling and remodeling studies[24,31,36]. In a fracture repair model, we reported that compared to controls, $gCbl^{YF}$ mice mounted a robust periosteal response, had increased bony callus formation, and increased periosteal osteogenic potential *in vitro*. Furthermore, the three-fold increase in periosteal thickness during mesenchymal progenitor activation correlated with a subsequent increase in osterix- and ALP-positive bone lining cells [37]. We employed bulk mRNA-sequencing to identify novel transcripts upregulated in gCbl^{YF} periosteal cells compared to controls that would account for the robust periosteal expansion. Our analysis found that many cWnt/β-catenin pathway-related genes were differentially regulated in gCbl^{YF}-derived periosteal cells compared to controls: The upregulated genes included Wnt ligands (*Wnt10a*, *Wnt5b*, *Wnt4*), Wnt-associated receptor (*Frzb*,), Wnt inhibitors/antagonists (*Sfrp2*, and *Notum*), and Wnt target gene (*Sp7*) while expression of *Lrp6* and *Sfrp* was downregulated (Fig.1a).

One of the most significantly upregulated genes in this data set was *Lgr6* (5.82-fold change, P-adj =1.75 E-156). The Lgr6 is an adult stem cell marker [14–16] and an atypical G-protein-coupled receptor protein (GPCR) [13] that modulates the activity of the canonical Wnt (cWnt) signaling[18,38]. Among the other members of this receptor family, *Lgr5* expression was downregulated in gCbl^{YF}-derived cells compared to controls, and there was no significant change in the expression of *Lgr4*. The differential expression of these Lgr family members in the gCbl^{YF} periosteal cells was confirmed by qRT-PCR (Fig.1b).

Lgr6 marks distinct stem cell populations in terms of location and function in the hair follicle, nail bed, and lung[16,21,39]. To determine *Lgr6* expression specifically in self-renewing skeletal stem cells (SSCs), we analyzed a recently published single RNA Seq data from the long bones derived from postnatal day 3 (0-month), 2-month, and 24-month-old mice [40]. Relative expression analysis in the SSC population showed that *Lgr6* was highly

expressed (log fold change =1.447, P-adj = 0.000426) in a most primitive subgroup of SSC identified as the "Root" cluster, which did not demonstrate a trajectory toward a specific identity. This cluster also expressed other known skeletal stem and progenitor cell markers in the osteochondrogenic lineage, including *Sox9* (log fold change = 4.688, P-adj = 0.0428), *Grem1* (log fold change = 2.808, P-adj =0.000831) and *Gli1* (log fold change = 0.880, P-adj = 0.749) (Fig. 1c). We also analyzed the microarray data of SSCs and bone–cartilage– stromal progenitors (BCSPs) derived from young, mature, and aged mice [33]. Among these populations, *Lgr6* expression was higher compared to *Lgr4* and *Lgr5*. Furthermore, *Lgr6* expression was minimally changed with age compared to other SSC markers (Fig. 1d). Together, this data indicates that *Lgr6* is expressed in mesenchymal stem/progenitor cells residing in long bones.

Lgr6 expression correlates with osteogenic differentiation of osteochondral progenitor cells

Wnt signaling regulates osteogenic differentiation [41], and Lgrs are known targets of Wnt signaling [17,42]. Rspo2 is secreted matricellular protein[43] and Rspo-Lgr interaction augments cWnt signaling by preventing the turnover of Wnt Frizzled (Fzd) receptors[23,44,45]. We found that the combined treatment of Wnt3a and Rspo2 of wild-type periosteal cells increased *Lgr6* expression 2.5-fold more than treating cells with Wnt3a or Rspo2 alone; in contrast, no upregulation was seen for *Lgr5* expression (Fig. 1e). *Lgr6* is dynamically expressed in calvaria- and bone marrow-derived mesenchymal cells during osteogenic differentiation *in vitro* [19,20]. We examined *Lgr6* expression in primary periosteal cells since the periosteum harbors osteochondral progenitors and is essential to homeostatic bone formation and fracture healing. In the early phase of osteogenic differentiation, we observed increased *Lgr6* expression with a corresponding increase in *Sp7* expression; Levels of *Sp7* and *Lgr6* expression were downregulated after 14 days of osteogenesis (Fig. 1f). This expression pattern mirrors studies showing that *Lgr6* is upregulated in mesenchymal cells upon osteoinduction but decreases during osteoblastic differentiation and maturation[19,20]. Lgr4, another Lgr family member studied in bone-specific contexts[46,47], did not demonstrate this dynamic expression. Together, these results suggest that Lgr6 has a specific temporal role in osteoblast differentiation.

Lgr6 expression is increased in response to fracture healing

We determined Lgr6 expression in a femur fracture model in the context of bone injury. For this purpose, mice with an inactivating EGFP-ires-CreET2 insertion into endogenous *Lgr6* allele were used [16,19]. *Lgr6*$^{EGFP-ires-CreERT2/+}$ mice were bred with a *tdTomato* fluorescent reporter mouse (*Lgr6*$^{EGFP-ires-CreERT2/+}$; *Ai9*). Using a short chase following a tamoxifen injection, we found that in uninjured bones, scarce tdTomato+ cells were visible by microscopy in the bone marrow and fewer tdTomato+ osteocytes were also visible in the cortical bone; no tdTomato+ cells were found in the periosteum (Fig. 2a). Five days after the injury, the periosteum was thickened near the fracture site, and there was an increase in the number of tdTomato+ cells in the cambium layer of the periosteum (Fig 2b). Fourteen days post fracture, we found td Tomato+ cells in the fracture callus. Interestingly, no tdTomato+ chondrocytes within the callus were visible (Fig 2f). Immunostaining with anti-osterix antibodies showed the colocalization of tdTomato+ cells with osterix+ cells in

the callus (Fig. 2h and i). Together, these results indicated that in response to bone injury, within the fracture callus, the number of Lgr6+ progenitor cells and their progeny was increased on newly formed bone; many of the tdTomato+ cells were also osterix+.

Lgr6-null mice are osteopenic

We utilized previously described *Lgr6*-null mice to determine a functional role for *Lgr6* in bone[16,19]. We confirmed that *Lgr6*-null mice lack transcriptional activity of the *Lgr6* gene in long bones, and Lgr6 protein was not detected in lysates of bone marrow stromal cell cultures derived from *Lgr6*-null mice (Supplementary Figure 1a and b). While *Lgr4*-null and *Lgr5*-null mice have severe skeletal abnormalities and neonatal lethality [48,49], our results show that *Lgr6*-null mice develop into healthy, fertile adults with no changes in body weight or mass at 5 months of age (Supplementary Figure 1c), suggesting that Lgr6 is not as developmentally important as Lgr4 or Lgr5. *Lgr6*-null mice do not have significant differences in bone volume at 3-months (data not shown); however, at 5-months, both male and female mice show decreased bone volume. Microcomputed tomography (μCT) was used to evaluate trabecular and cortical bone parameters of the right distal femur at all time points for both sexes. At five months of age, *Lgr6*-null mice had a decrease in trabecular BV/TV compared to their control sex-matched littermates (BV/TV, males = −49%, P=0.035; females = −85% P=0.045) (Fig.3b). The decreased BV/TV corresponded to decreased trabecular number (45% and 35% decrease in male and female mice respectively) and increased trabecular spacing (males= 2-fold; females=1.6-fold); trabecular thickness was not changed in males, and there was a 20% increase in *Lgr6*-null females (P= 0.0376) (Fig. 3; Table1). Compared to controls, in *Lgr6*-null mice, the cortical porosity was decreased (Ct. Po, males 34.4%, P=0.0001; females 27%, P= 0.0087), while no significant differences were identified in the cortical bone area or thickness (Table 1). Despite a decrease in the trabecular bone volume, there were no changes in *Col1a*, *Runx2*, or *Axin2* gene expression in the femurs of 5-month-old *Lgr6*-null mice (Supplementary Figure 1d).

Skeletal progenitors isolated from *Lgr6-null* mice have reduced colony-forming potential and reduced osteogenic differentiation capacity due to attenuated cWnt signaling

Using *ex vivo* cultures, we evaluated the colony-forming capabilities of mesenchymal cells harvested from bone marrow and periosteum to assess the cellular basis for the decreased bone volume. *Ex vivo*, periosteal progenitors derived from *Lgr6*-null mice showed a significant decrease in CFU-F (Control = 56.3, *Lgr6*-null = 26.6, P=0.001) and CFU-ALP+ (Control= 31.6, *Lgr6*-null =12.6, P= 0.0005) (Fig. 4a–c). We also found that at 3- and 5 months of age, there was a 40% and 36 % decrease in CFU-Fs from *Lgr6*-null bone marrow-derived cells, indicating reduced *in vitro* progenitor potential. In addition, *Lgr6*-null cells also had a significant deficiency in CFU-ALP, which was more pronounced with age. While cells from control animals successfully formed numerous ALP+ colonies, in *Lgr6*-null cultures, there was a 50% decrease in CFU-AP at 3 months. Remarkably, *Lgr6*-null cultures derived from 5-month-old mice had only 0–2 CFU-ALP+ colonies (Fig. 4f).

Strikingly, *Lgr6*-null-derived periosteal cells also show severely impaired osteogenic differentiation as evaluated by ALP staining and alizarin red staining of calcium deposits (Fig. 4g). *Lgr6*-null-bone marrow stromal cells from 3-month-old mice also exhibit

significant deficiencies in mineralization, while cells from control animals of the same age successfully differentiate into mature, mineral-depositing osteoblasts after 21 days of differentiation (Fig. 4g). This impaired osteogenic capacity is also evident with decreased expression of osteogenic markers, including *Runx2, Alpl, Ocn*, and *Col1a1* (Fig. 4i and Supplementary Figure 2). Consistent with the role of Lgr6 in modulating Wnt signaling, we found that compared to controls, *Lgr6*-null cultures exposed to Wnt3a had 67% and 25% decrease in *Axin2* and *Lef1* expression, respectively (Fig. 4j). We confirmed no changes in the potential to differentiate toward the chondrocytic lineage (Supplementary Figure 2). As reduced bone mass could be due to increased osteoclast activity, we assessed *in vitro* osteoclastogenesis assays using bone marrow-derived monocytes (BMMs). We found no differences in the number of osteoclasts in cultures from *Lgr6*-null mice and controls (Supplementary Figure 2).

Lgr6-null mice have a lower proportion of skeletal stem cells

We used the flow cytometry technique to discern further how Lgr6 modulates progenitor cell populations. We utilized cell surface antigen combinations and gating strategies developed in the Chan and Longaker laboratories to identify skeletal stem cells and their downstream bone, cartilage, and stromal progenitors [50]. Using this strategy, we evaluated the presence of three distinct populations of skeletal progenitors, which exist in a differentiation hierarchy: self-renewing stem cells (SSC, CD45−Ter119−CD31 −Thy1−6C3−CD51+CD105−CD200+) at the apex and two populations of downstream, more committed progenitors pre bone–cartilage–stromal progenitor (pre-BSCP, CD45−Ter119−CD31 −Thy1−6C3−CD51+CD105−CD200-) and bone–cartilage–stromal progenitors (BSCP, CD45−Ter119−CD31−Thy1−6C3−CD51+) (Fig. 5). Our analysis showed that bone marrow and periosteal cells isolated from *Lgr6*-null mice display a significant shift in the proportion of these populations compared to controls; specifically, a smaller percentage of the subpopulation of self-renewing SSCs in bone marrow (SSC, Control 0.172% SD± 0.38, *Lgr6*-null 0.073 SD ± 0.019, P = 0.0072) and periosteum (SSC, Control 1.805% SD± 0.058, *Lgr6*-null 1.046 SD ± 0.461, P= 0.019). Surprisingly, we found an increase in the percentage of Pre-BSCP in *Lgr6*-null samples (Pre-BSCP, Control =16.8%, *Lgr6*-null = 22.1, P = 0.017) while the number of BSCP was comparable between the genotypes. We also evaluated widely used mesenchymal progenitors marked by Sca1, CD140a, and CD105, to identify mixed populations of mesenchymal progenitor cells. *Lgr6*-null derived bone marrow had fewer CD140a+ (CD140a+, Control = 3.22%, SD ±1.019; *Lgr6*-null =1.54 SD ± 0.47, P =0.012) and CD105+ cells (CD105+, Control = 20.87%; *Lgr6*-null =14.6, P=0.003). *Lgr6*-null periosteal cells also showed a decrease in the expression of CD140a+ cells (CD140, Control = 9.14%; *Lgr6*-null 5.25%, P =0.039). We observed no changes in CD105+ cells in the periosteum. The frequency of Sca1+ cells was comparable between the genotypes in both compartments (Fig. 5e and data not shown).

Lgr6-null mice show deficient proliferation and ALP activity immediately after fracture injury

To determine a functional role for Lgr6 in response to injury, a closed, stabilized, femoral fracture model of bone healing, an established method to evaluate endochondral

regeneration, was used [24,37,51,52]. To avoid the influence of the reduced bone formation evident at 5 months of age, we employed 3-month-old male and female mice, which do not have any overt skeletal phenotype (data not shown). Upon initiation of fracture repair, skeletal progenitors are activated at the fracture site, and periosteal cells respond to injury within 24–48 h post-injury [10,52,53]. At 3 days post-fracture, relatively fewer EdU$^+$ cells were observed in the periosteum of fractured femurs in Lgr6 null mice compared to controls (EdU$^+$ cells, Controls 24%, *Lgr6*-null 13%, P=0.0023) (Fig. 6a). We also analyzed alkaline phosphatase activity; In intact contralateral femurs, ALP activity in the periosteum was comparable between the genotypes. However, 3- and 5-days post-fracture injured periosteum in *Lgr6*-null mice showed a 60% and 48% decrease, respectively, in the ALP$^+$ activity relative to control mice (Fig. 6b). Flow cytometric analysis of mesenchymal progenitors in the periosteum derived from fractured femurs from *Lgr6*-null mice showed 48% decrease in SSCs (P=0.048) and 32% increase in pre-BCSP (P=0.030) populations. In comparison, no changes were observed in the BSCP population (Fig. 6c).

Lgr6-null mice have impaired endochondral fracture healing

Following a femoral fracture, we analyzed the calluses during the bone regeneration phase (14 days post-fracture) and remodeling phase (28 days post-fracture) to evaluate healing in *Lgr6*-null mice and control mice. Overall callus size 14 days post-fracture was comparable among groups, but *Lgr6*-null calluses had significantly reduced bone content/volume relative to controls. Reconstructed images from µCT scanning demonstrated the presence of large unmineralized voids in *Lgr6*-null fracture calluses (Fig. 7a). µCT analysis showed that *Lgr6*-null mice had significantly reduced callus BV/TV as compared to control (BV/TV, Control = 22.3 %; *Lgr6*-null = 15.47%, P=0.019). Additional analysis revealed a 22% decrease in bone mineral density (BMD) in *Lgr6*-null fracture calluses compared to controls (Fig. 7b). Safranin O staining and cellular morphology indicated that these voids were composed of cartilaginous tissue and that *Lgr6*-null calluses had retained 41% more cartilage content compared to the controls at this phase of fracture repair, lacking the robust mineralization capacity of control samples (Fig. 7c and d).

During the regeneration phase, in areas flanking the central fracture callus, we observed successful new bone formation in the *Lgr6*-null samples in histological sections and via µCT. TRAP staining and quantification showed no differences in the number of osteoclasts or osteoclast surfaces compared to the total bone surface in these areas of ossification, flanking the fracture site (Fig. 7e and f). To indirectly evaluate the *in vivo* osteogenic activity of osteoblasts in these areas of the calluses, we injected calcein one day before animal sacrifice to label the active bone surfaces (Fig. 7g and h). We found that even in areas of mineralization within the *Lgr6*-null calluses, there was reduced osteoblast activity compared to controls, as evident from the mineralization pattern and the quantified integrated density of calcein fluorescence within these defined regions of interest (Control =186; *Lgr6*-null = 101, P =0.025).

We then evaluated the remodeling phase of fracture healing to observe the calluses' ability to ossify and eventually remodel. We found that the *Lgr6*-null calluses ultimately mineralized successfully (Fig. 8a). However, *Lgr6*-null calluses had 25% reduced bone

volume fraction and 23% decreased bone mineral density compared to controls, as measured by μCT (Fig. 8b). Additionally, the healing bones of *Lgr6*-null mice continued to display aberrant morphology compared to controls, with significantly larger calluses in terms of total volume (TV mm^3 Control= 7.98 ± 4.73; *Lgr6*-null = 22.1 ± 6.98, P=<0.0001), but the very sparse formation of new trabeculae. Safranin O staining confirmed the complete lack of cartilaginous matrix within the calluses, and a counterstain with fast green showed fewer and thinner areas of newly formed bone in *Lgr6*-null-derived samples compared to controls, corroborating with μCT data (Fig. 8c). TRAP staining of defined regions within these calluses revealed significantly more osteoclasts per bone surface (N.Oc./BS, Control = 6.3; *Lgr6*-null = 10.9, P= 0.005) present in the day 28 post-fracture *Lgr6*-null calluses (Fig. 8d). A calcein label showed increased osteoblast activity (Control = 70; *Lgr6*-null = 119, P= 0.0002) in the *Lgr6*-null calluses compared to control (Fig. 8e). These results combined demonstrated higher bone remodeling activity in *Lgr6*-null calluses, while control calluses remodeled and closer to complete healing, overall indicating delayed healing progression.

Discussion

In this study, we report that Lgr6 is distinct among the three Lgr family members found in mammals, as it is associated with regeneration and osteogenic capacity rather than skeletal development. Our studies demonstrate that despite representing a small fraction of the total population, *Lgr6*-null mice experience a significant delay in callus mineralization and fracture healing. Importantly, in strong support of our work examining the role of Lgr6 in fracture healing, a recent RNA expression analysis of the mesenchymal stem cells derived from fractured bones of patients with hip fractures found that *LGR6* was the most upregulated gene (Fold change 11.0, corrected P-value =0.0083) [54]. Furthermore, separate GWAS studies have shown that variants associated with *LGR4* and *LGR6* loci are correlated with low BMD, osteoporosis risk, and osteoporotic fractures [55,56]. In addition, human genetic studies showed that increased *RSPO3* expression is associated with increased trabecular bone mineral density and reduced risk for fractures[46]. Combined, these studies underscore the role of the Rspo/Lgr axis in bone regeneration.

We discovered that the expression of *Lgr6* and many components of cWnt signaling was increased in periosteal cultures derived from a mouse model, which has increased PI3K-AKT activation. Interestingly, LGR6 was also reported to function as an anti-apoptosis protein controlling the progression of gastric cancers through PI3K/AKT/mTOR pathway[57]. PI3K-AKT signaling forms a major signaling node downstream of growth factors and cytokines involved in fracture healing and bone stress[24,53,58]. In our working model (Supplementary Figure 3), we propose that PI3K-AKT activation in response to injury, results in the phosphorylation of GSK3, a serine/threonine kinase that plays a central role in the regulation of the Wnt/β-catenin signaling pathway. In the resting state, GSK3 phosphorylates β-catenin, triggering its destabilization and degradation to maintain a very low level of β-catenin in the cytosol/nucleus. AKT-mediated phosphorylation of GSK3 activity leads to stabilization and activation of β-catenin and TCF/LEF-dependent gene transcription, and expression of Wnt target genes, including *Lgr6*. Based on our work shown here, we propose that in osteoprogenitor cells, Lgr6 expression is increased due to enhanced

Wnt activity; binding of Lgr6 to Rspondin2/3 potentiates cWnt signaling in a positive feedback loop promoting osteogenesis during healing.

The regeneration phenotype in *Lgr6*-null mice is due to a 40–50% decrease in cell proliferation at the periosteum during the initial phase of fracture healing and a defect in osteogenic capacity and osteoblast differentiation. In the *Lgr6*-null mice, which have decreased frequency of SSCs, muted cWnt response likely results in decreased proliferation and differentiation of periosteal osteoprogenitors. Together, these deficits contribute to impaired bone formation during the early phases of healing. A negative effect on osteogenesis results in lesser or delayed stabilization of the callus leading to increased chondrogenesis. Although we found a significant increase in the cartilaginous bone at day 14, there was no detrimental effect on the cartilage-to-bone transition [59,60], as calluses of Lgr6-null fractured bones eventually ossify successfully. Using Lgr6+/Ai9, we observed an increase in Lgr6+ cells and their progeny in the injured periosteum differentiated into osteoblasts. We also found that *in vitro* chondrogenesis in *Lgr6*-null mice was also normal. The Lgr6-null fracture phenotype contrasts with other fracture healing studies reporting the impairment of successful cartilage differentiation during bone healing, for example, in a mouse model with an over-activating mutation of *Fgfr3* in Prx1-derived progenitors[61]. In this study, periosteal cells with the *Fgfr3* mutation do not undergo expected terminal chondrocyte hypertrophy following transplantation [62,63], leading to failure of fractures to consolidate; the chondrocytes fail to hypertrophy and terminally differentiate, and there is persistent fibrosis within the callus day 28 post-fracture. In our study, calluses from *Lgr6*-null animals at day 28 post-fracture are still being heavily remodeled and have less mineralized tissue content due to delays in the healing process; however, there is no evidence of fibrosis or cartilage remnants at this time point.

Lgr6+ cells in injured periosteum are likely a subpopulation of skeletal stem/progenitors identifying a unipotential osteoprogenitor. This model differs from the previously reported markers[5,11,12,64], which differentiate into osteoblasts and chondrocytes in response to fracture. Whether the bipotentiality of periosteal skeletal stem progenitor cells in fracture response is due to the presence of a single lineage or multiple lineages is unclear, or if this plasticity is regulated by the fracture environment and factors mediating injury response remains to be answered. Our flow data shows Lgr6-null mice have a smaller proportion of SSC than controls, but there is an increase in the pre-BSCP population. One possibility is that Lgr6-responsive stem/progenitor cells control "stemness" by maintaining the expression of inhibitors of differentiation. The concept of an anti-differentiation program regulating stemness is intriguing; future studies will provide new information.

In Lgr6-null cultures, we found no changes in osteoclast differentiation but demonstrated decreased ALP+ colonies, osteogenic differentiation, and mineralization; therefore, we attribute the decreased trabecular bone volume in Lgr6-null mice to reduced bone formation by osteoblasts. The Lgr6-null trabecular phenotype is more pronounced than the cortical phenotype. While the quantity of cortical bone was unchanged in Lgr6-null animals, we identified a decrease in cortical porosity. In our lineage tracing studies using *Lgr6$^{EGFP\text{-}ires\text{-}CreERT2/+}$; Ai9* mice, we found few Tomato+ osteocytes; using the same mouse similar findings were also reported by others[19]. The reduced cortical porosity could be

associated with decreased cortical remodeling due to reduced osteocyte function in *Lgr6*-null mice. However, higher resolution scans would be needed to characterize osteocyte lacunae. Other models of deficient Wnt signaling, including Wnt10B [65], Wnt16 [66–68], Notum [69], Rspo2[70], and Rspo3[46,] also have shown a discrepancy between trabecular and cortical bones. Future studies in *Lgr6*-null mice at geriatric time points are needed to examine the effect of Lgr6 on cortical bones. In agreement with our studies, another global Lgr6 knockout mice with a deletion in exons 15 and 16 showed a decrease in bone volume in both sexes compared to control cohorts at 2 months of age, but no changes were found in cortical bone parameters [19]. In our studies, mice lacking endogenous *Lgr6* expression at 3 months of age had no overt skeletal phenotype, likely due to the compensatory effect by other Lgr family members [71,72]; however, with age, this compensation is insufficient in maintaining bone volume. Further, this compensatory mechanism is not evident upon injury since fracture healing is significantly impaired in 3-month-old *Lgr6*-null mice. Together, these data support the notion that Lgr6+ osteoprogenitors are activated in response to bone injury.

The effect of Wnt signaling on regulating osteoprogenitors is complex: the disruption of cWnt signaling decreases progenitor number in the Lrp5-knockout, Wnt10b-knockout, Rspo2 knock out models [65,70,73] but high levels of expression of stabilized beta-catenin also reduced the number of CFU-F colonies [74]. While no difference in Axin2 or b-catenin expression (data not shown) was observed in long bones of *Lgr6*-null mice, *in vitro* studies showed that in *Lgr6*-null cells in response to Wnt3a stimulation, expression of Wnt response genes, *Axin2* and *Lef1* was attenuated. However, the levels of these proteins also depend on the osteogenic differentiation; therefore, a direct comparison of Wnt signalosome components between *Lgr6*-null cells and controls following osteogenic induction may still not lead to a definitive answer, as *Lgr6*-null cells have impaired osteogenic differentiation *in vitro*. Thus, it will be difficult to interpret if the results are due to alterations in Wnt signaling or osteogenic differentiation potential by another mechanism unassociated with Wnt. Nevertheless, it cannot be ruled out that *Lgr6* acts in a currently unidentified, Wnt-independent mechanism, especially considering recent reports on Lgr family member involvement in different signaling pathways, including ERK/FGF, BMP2, and BMP9 [47,75,76].

Currently, known ligands for Lgr6 include R-spondins and Maresin 1 (MaR1). MaR1 delivery to tibial fractures enhanced bone healing [77], and while MaR1 can bind Lgr6 [78,79], studies are needed to demonstrate a MaR1/Lgr6 interaction specifically within osteoblast lineage. Rspo2 is an essential regulator of bone mass[70], and various Rspos may enhance osteogenic differentiation *in vitro*[44,80,81]. However, Rspos have binding affinity for all three Lgr family members, and it remains unclear if a distinct Rspo/Lgr6 axis regulates osteoblast differentiation [38]. Further, Rspo2 is a possible ligand within the BMP pathway, which may be another mechanism by which it enhances osteogenesis [75].

Our lineage tracing studies have some limitations. Despite the inclusion of a GFP reporter in the Lgr6$^{EGFP-ires-CreERT2}$ model, a direct comparison between *Lgr6*-positive progenitors and *Lgr6*-negative progenitors was not performed. Since we were unable to isolate GFP+ cells due to a very weak signal and a lack of available antibodies appropriate for use in

these applications. The Lgr6$^{EGFP\text{-}ires\text{-}CreERT2}$ model is a low-efficiency Cre mouse model; we found that under homeostatic/non-injured conditions, tamoxifen induced fewer numbers of Lgr6+ cells in the bone compartment. While there are significantly increased numbers of Td tomato+ cells in fracture callus, a new mouse model to use as a lineage tracing tool that more faithfully marks Lgr6+ cells upon tamoxifen induction would be informative.

Methods

Mice

Cbl$^{YF/YF}$ mice (gCbl^{YF}) were described previously [25]. Mice with knock-in targeted insertion of the EGFP-Ires-CreERT2 into the Lgr6 transcriptional start of *Lgr6* locus (*Lgr6$^{EGFP\text{-}IRES\text{-}CreERT2}$*) were bred into a mixed 129/SV background [16]. Heterozygous breeding of these knock-in mice into homozygotes yields *Lgr6$^{EGFP\text{-}IRES\text{-}CreERT2/}$* *Lgr6$^{EGFP\text{-}IRES\text{-}CreERT2}$* (henceforth *Lgr6*-null mice), *Lgr6$^{EGFP\text{-}IRES\text{-}CreERT2/+}$* and control littermates; functional endogenous *Lgr6* expression is blocked from both alleles in *Lgr6*-null mice [16]. *Lgr6*-null and *Lgr6$^{EGFP\text{-}IRES\text{-}CreERT2/+}$* mice developed normally with no overt developmental phenotype[39]. In *Lgr6EGFP-ires-creERT2/+* mice, due to extremely weak IRES reporter, we do not see GFP+ cells in either bone sections or bone cells by histology and flow cytometry (data not shown). In our studies, we compared *Lgr6*-null and control mice since we found no difference in the skeletal phenotype of control and *Lgr6$^{EGFP\text{-}IRES\text{-}CreERT2/+}$* mice of either sex at 3- or-5 months of age (data not shown). For lineage tracing experiment, *Lgr6$^{EGFP\text{-}IRES\text{-}CreERT2/+}$* were bred with Ai9 tomato reporter (Ai9 (B6. Cg-Gt (ROSA) 26Sor$^{tm9(CAG\text{-}tdTomato)\ Hze}$/J). Both male and female mice were used as indicated. Genotyping for mice was performed at the time of weaning and before each experiment using Lgr6-specific primers listed in Supplementary Table 1.

Animal Welfare

This study was approved by the local IACUC and was conducted per the national legislation on the protection of animals and the NIH Guidelines for the Care and Use of Laboratory Animals. All animals were housed in ventilated cages in a temperature- and the humidity-controlled environment under a 12-hour light cycle.

µCT analysis

Structural analysis of intact and fractured femurs was performed using cone-beam x-ray microcomputed tomography (µCT40, Scanco Medical AG) at the µCT Imaging Facility at UConn Health. Scans with an isotropic voxel size of 8µm were acquired at 55kVp, 145 and µA, 1000 projections with a Gaussian filter. The instrument is calibrated using Scanco phantoms. Intact femurs were analyzed at the microCT Core at UConn Health, with lower thresholds of 270 per mille (449.4mgHA/ccm) for trabecular bone and 400 per mille (748.2mgHA/ccm) for cortical bone. Fractured femurs were analyzed by manually segmenting callus tissue from surrounding bone[82], with a lower threshold of 270 per mille (403.3mgHA/ccm).

Cell isolation

Bone marrow and periosteal cells were isolated from femurs and tibias as previously described [37]. For periosteal cultures, 2–3 mice of the same sex and genotype were pooled to get enough cells. Briefly, the periosteum was scraped from flushed, hollow bones into sterile PBS and digested enzymatically (0.05% collagenase P, 0.2% hyaluronidase in PBS) for one hour at 37° C in an orbital shaker. Then, complete media was added to stop enzymatic digestion, and cells were filtered through a 40 μm mesh strainer to form a single-cell suspension and remove debris. Cells were grown in 5% oxygen for 4 days to allow for expansion before transfer to 20% oxygen.

CFU Assays

Colony-forming unit (CFU) assays were performed using bone marrow-derived and periosteum-derived cells. Cells were isolated as described above. Bone marrow-derived cells from individual mice were directly plated at 1×10^6 cells 60 mm culture plates in duplicates and cultured for 10 days in 20% oxygen without cell passage. Periosteal cells were pooled from two mice of the same sex, age, and genotype for each biological replicate for appropriate cell numbers. Cells were plated at 5×10^5 cells per well in 60 mm plates in duplicates and cultured for 4 days in 5% oxygen, followed by 4 days in 20% oxygen without cell passage. Fixed cells were stained either for ALP activity using an ALP detection kit according to the manufacturer's instructions (Sigma-Aldrich) or with crystal violet. Colonies were imaged using a Leica microscope and were evaluated using converted greyscale 8-bit images in ImageJ

Cell differentiation and staining

For osteogenic differentiation, periosteal- and bone marrow-derived cells were seeded (2×10^5 cells/well) in 12-well plates. Cells were treated with differentiation media (50 μg/mL ascorbic acid, 4 mM β-glycerophosphate) once cells reached 80–90% confluence in culture in about 2–3 days. Media was changed every other day for 7, 14, and 21 days. Cultures were stained to detect ALP activity as described above. Cells were fixed in cold methanol and stained with Alizarin Red S (Science Cell) to visualize *in vitro* mineralization. Staining was quantified according to the manufacturer's instructions using colorimetric detection. Osteogenic differentiation was repeated at least three times per time point to confirm ossification trends. For chondrogenic assays, periosteal bone marrow-derived cells were seeded in 12-well plates were treated with chondrogenic differentiation media starting when cells reached 80–90% confluence, as we have previously described[37]. Media was replaced every other day for the remainder of the assay. After 14 days, cells were either harvested to isolate RNA or were fixed and stained with Alcian blue to assess chondrocytic differentiation. Osteoclast cultures were established and evaluated as previously described[82].

Bulk mRNA sequencing and analysis

RNA was isolated from cell cultures using a Trizol (Invitrogen) extraction method. Total RNA was quantified, and purity ratios were determined for each sample using the NanoDrop 2000 spectrophotometer (Thermo Fisher Scientific). To further assess RNA quality, total RNA was analyzed on the Agilent TapeStation 4200 (Agilent Technologies) using the

RNA High Sensitivity assay. Only samples with RINe values above 8.0 were considered for library preparation. Illumina Transcriptome Library preparation and Sequencing Total RNA samples were prepared for mRNA-Sequencing using the Illumina Stranded mRNA Ligation Sample Preparation kit following the manufacturer's protocol (Illumina). Libraries were validated for length, and adapter dimer removal using the Agilent TapeStation 4200 D1000 High Sensitivity assay (Agilent Technologies), then quantified and normalized using the dsDNA High Sensitivity Assay for Qubit 3.0 (Life Technologies). Sample libraries were prepared for Illumina sequencing by denaturing and diluting the libraries per the manufacturer's protocol (Illumina). All samples were pooled into one sequencing pool, equally normalized, and run as one sample pool across the Illumina NovaSeq 6000 using version 1.5 chemistry. A target read depth of 50 M reads was achieved per sample paired-ended end 100bp reads. Raw reads were trimmed with FASTP 96 (version 0.23.0), with low-quality sequences removed, and trimmed reads mapped to Mus 97 musculus genome (GRCm39) with HISAT2 (version 2.1.1). SAM files were then converted into BAM 98 format using samtools (version 1.12), and the PCR duplicates were removed using PICARD 99 software (http://broadinstitute.github.io/picard/). Counts were generated against the features with 100 htseq-count. Differential expression of genes between conditions was evaluated using DESeq2 101.

RNA isolation and cDNA synthesis for qPCR

Total RNA was extracted from cultured cells and freshly dissected tibia. For tibial RNA extraction, both ends of each tibia were cut off to remove the growth plates, and the marrow was flushed by centrifugation at 300 g for 1 minute at 4°C. Both tibiae from one mouse were pooled and homogenized in TRIzol (Invitrogen). Tissue RNA integrity was checked on BioAnalyzer RNA NanoChips (Agilent Technologies) at the UConn Health molecular core facility. Only samples with a RIN value of <8.0 were used. cDNA synthesized using Superscript III cDNA synthesis kit (Invitrogen). qRT-PCR reactions were performed on a Bio-Rad real-time PCR system using SYBR Green (BioRad) PCR reagents. For each gene of interest, qPCR was performed in both technical and biological triplicates. Data were normalized to GAPDH or beta-actin. The 2^{-DDCt} method was used to calculate the relative gene expression. Primer sequences are listed in Supplementary Table 1.

Assessment of cWnt Signaling

To analyze the expression of genes by real-time PCR, bone marrow stromal cells were cultured to confluence, serum starved for 12h, and then treated with Wnt3a (50ng/ml) (R and D systems). Seventy-two hours after treatment, cells were lysed with Trizol (Life Technologies) and frozen at −80° C. Subsequently, RNA was extracted, and qRT-PCR was performed using Axin2 and Lef1 primers listed in Supplementary Table 1.

Flow Cytometry

Bone marrow cells were isolated from each mouse as one biological replicate. For periosteum-derived preparations, cells from 2–3 mice were pooled. For fractured samples, 2–3 fractured femurs were pooled. In all cases, after cell isolation, red blood cell lysis was performed in ACK buffer (Sigma). For each sample, 1×10^6 cells were collected in cell staining media containing HEPES and 2% heat-inactivated FBS in Hanks Balanced Salt

Solution (HBSS). Cells were incubated with antibodies and secondary reagents indicated in Supplementary Table 2. Cells were incubated with an antibody cocktail for 45 minutes on ice and then washed in ice-cold staining media. Dead cells were excluded using Live IR staining. Cells were analyzed using a BD-LSRII flow cytometer (BD Biosciences). All experiments included unstained bone marrow and periosteal cells for establishing gates. Fluorochrome beads were used as single-color controls. In some experiments, fluorescence minus one (FMO) control was used to assist in gating. Experiments included 5–6 biological replicates and were performed twice to ensure consistent outcomes.

Surgical Procedures

Closed, stabilized femoral fractures were generated as previously described in 10-week-old mice[37,51,52]. Briefly, pin placement was confirmed using a Faxitron Cabinet X-Ray system (Faxitron Corporation), and the femur was fractured using an Einhorn three-point drop-weight device and evaluated using X-ray. Buprenorphine (0.1 mg/kg body weight) was administered by subcutaneous injection before the procedure and twice a day for three days following the fracture for pain management. Samples excluded from the study analysis included multi-fracture, bent pins, and fracture placement that was not mid-diaphyseal. Both male and female mice were used in fracture healing experiments, and mice were euthanized 3, 5, 1428 days8-days post-fracture for analysis.

Histology

To activate the inducible Cre in the Lgr6[EGFP-ires-CreERT2]/+; Ai9/+ mouse model, tamoxifen (10 mg/mL, Sigma-Aldrich) in corn oil or vehicle was administered intraperitoneally at a dosage of 75 μg/g body weight in 10–12-week-old-mice, and long bones were harvested 5 and 14 days after injection. In some experiments, tamoxifen was administered one day before and the day of fracture, and mice were sacrificed for histological analyses 5- and 14-days following fracture surgery. Bones were processed for frozen sectioning as previously described[40]. Fluorescent images were visualized using either Axioscan slide scanner (Zeiss) or Nikon Eclipse 50i microscope. For Osterix staining, sections were permeabilized in 0.1% Tween-20 in PBS for 15 minutes, then blocked in 10% goat serum and 2% BSA in PBS for 1 hr. Sections were stained with anti-Osterix antibodies overnight at 4 C. Sections were washed in 0.1% Tween in PBS and stained with secondary antibody for 1 hour at room temperature.

To visualize remodeling fracture calluses, calcein was injected (10 mg/kg body weight IP) one day before sacrifice to label active areas of bone formation. A small piece of the tail was clipped to visualize the presence of dyes on the day of the injection . The integrated density of the calcein fluorescent label was quantified in ImageJ. Measurements were taken from four different sites of intramembranous bone formation, flanking the fracture site of each sample, and averaged.

To assess cell proliferation, mice were injected with 5-ethynyl-2'-deoxyuridine (EdU) (10mM) in normal saline 24 hours before sacrifice to measure cell proliferation. Fractured and intact contra lateral femur sections were stained for EdU labeling using the Click-iT® EdU Alexa Fluor® 488 Imaging Kit (Life Technologies) according to the manufacturer's

instructions. ALP activity post-fracture was evaluated using a modification of the ALP Leukocyte kit (86R-1KT) (Sigma) with Fast Blue-BB salt (F3378). ALP+ periosteal area was quantified using methods described previously [30]. RGB images were split into the three-color channel 8-bit images. The red channel 8-bit image was analyzed further for positive pixels in the region of interest (ROI) in the periosteum, above the threshold of 55 for intact femurs and 85 for D3 fractured femurs. Data are presented as a percentage of ALP+ positive pixels over the threshold, normalized to total pixels in the ROI measured.

To visualize morphology and detect cartilage content, fixed and decalcified samples were paraffin-embedded decalcified bone sections were cut at 7 μm on a microtome, sections were deparaffinized, stained with safranin O/fast green, and counterstained with hematoxylin to detect cartilage content. Tartrate-resistant acid phosphatase (TRAP) staining was performed to visualize osteoclasts in fractured bones. Sections were analyzed using Osteomeasure[30,40] to measure the number of TRAP+ osteoclasts, osteoclast surface, and bone surface in regions of interest.

Statistical Analyses

Experiments conducted for this study were repeated at least three times or were presented with biological replicates. Statistical analyses were performed using GraphPad Prism v6 software with either a student's t-test or one-way ANOVA with Tukey's post hoc test comparing the control group to *Lgr6*-null-mice. Data are presented as mean ± SD. *P-values* < 0.05 were considered statistically significant.

Supplementary Material

Refer to Web version on PubMed Central for supplementary material.

Acknowledgments

References

1. Tzioupis C & Giannoudis PV Prevalence of long-bone non-unions. Injury 38 Suppl 2, S3–9 (2007). 10.1016/s0020-1383(07)80003-9

2. Claes L, Recknagel S & Ignatius A Fracture healing under healthy and inflammatory conditions. Nat Rev Rheumatol 8, 133–143 (2012). 10.1038/nrrheum.2012.1 [PubMed: 22293759]

3. Clark D, Nakamura M, Miclau T & Marcucio R Effects of Aging on Fracture Healing. Curr Osteoporos Rep 15, 601–608 (2017). 10.1007/s11914-017-0413-9 [PubMed: 29143915]

4. Kalaitzoglou E, Popescu I, Bunn RC, Fowlkes JL & Thrailkill KM Effects of Type 1 Diabetes on Osteoblasts, Osteocytes, and Osteoclasts. Curr Osteoporos Rep 14, 310–319 (2016). 10.1007/s11914-016-0329-9 [PubMed: 27704393]

5. Duchamp de Lageneste O et al. Periosteum contains skeletal stem cells with high bone regenerative potential controlled by Periostin. Nat Commun 9, 773 (2018). 10.1038/s41467-018-03124-z [PubMed: 29472541]

6. Marecic O et al. Identification and characterization of an injury-induced skeletal progenitor. Proc Natl Acad Sci U S A 112, 9920–9925 (2015). 10.1073/pnas.1513066112 [PubMed: 26216955]

7. Marsell R & Einhorn TA The biology of fracture healing. Injury 42, 551–555 (2011). 10.1016/j.injury.2011.03.031 [PubMed: 21489527]

8. Colnot C Skeletal cell fate decisions within periosteum and bone marrow during bone regeneration. Journal of bone and mineral research : the official journal of the American Society for Bone and Mineral Research 24, 274–282 (2009). 10.1359/jbmr.081003 [PubMed: 18847330]

9. Colnot C, Zhang X & Knothe Tate ML Current insights on the regenerative potential of the periosteum: molecular, cellular, and endogenous engineering approaches. Journal of orthopaedic research : official publication of the Orthopaedic Research Society 30, 1869–1878 (2012). 10.1002/jor.22181 [PubMed: 22778049]

10. Matthews BG et al. Analysis of αSMA-labeled progenitor cell commitment identifies notch signaling as an important pathway in fracture healing. J. Bone Miner. Res 29, 1283–1294 (2014). 10.1002/jbmr.2140 [PubMed: 24190076]

11. Grcevic D et al. In vivo fate mapping identifies mesenchymal progenitor cells. Stem Cells 30, 187–196 (2012). 10.1002/stem.780 [PubMed: 22083974]

12. Ortinau LC et al. Identification of Functionally Distinct Mx1+alphaSMA+ Periosteal Skeletal Stem Cells. Cell Stem Cell 25, 784–796 e785 (2019). 10.1016/j.stem.2019.11.003 [PubMed: 31809737]

13. Hsu SY et al. The three subfamilies of leucine-rich repeat-containing G protein-coupled receptors (LGR): identification of LGR6 and LGR7 and the signaling mechanism for LGR7. Mol Endocrinol 14, 1257–1271 (2000). 10.1210/mend.14.8.0510 [PubMed: 10935549]

14. Barker N et al. Identification of stem cells in small intestine and colon by marker gene Lgr5. Nature 449, 1003–1007 (2007). 10.1038/nature06196 [PubMed: 17934449]

15. Clevers H, Loh KM & Nusse R Stem cell signaling. An integral program for tissue renewal and regeneration: Wnt signaling and stem cell control. Science 346, 1248012 (2014). 10.1126/science.1248012 [PubMed: 25278615]

16. Snippert HJ et al. Lgr6 marks stem cells in the hair follicle that generate all cell lineages of the skin. Science 327, 1385–1389 (2010). 10.1126/science.1184733 [PubMed: 20223988]

17. Glinka A et al. LGR4 and LGR5 are R-spondin receptors mediating Wnt/beta-catenin and Wnt/PCP signalling. EMBO Rep 12, 1055–1061 (2011). 10.1038/embor.2011.175 [PubMed: 21909076]

18. Lehoczky JA & Tabin CJ Rethinking WNT signalling. Nature 557, 495–496 (2018). 10.1038/d41586-018-04820-y [PubMed: 29777190]

19. Khedgikar V, Charles JF & Lehoczky JA Mouse LGR6 regulates osteogenesis in vitro and in vivo through differential ligand use. Bone 155, 116267 (2022). 10.1016/j.bone.2021.116267 [PubMed: 34856421]

20. Khedgikar V & Lehoczky JA Evidence for Lgr6 as a Novel Marker of Osteoblastic Progenitors in Mice: LGR6 AS A MARKER OF OSTEOPROGENITORS. JBMR Plus (2018). 10.1002/jbm4.10075

21. Lee JH et al. Anatomically and Functionally Distinct Lung Mesenchymal Populations Marked by Lgr5 and Lgr6. Cell 170, 1149–1163 e1112 (2017). 10.1016/j.cell.2017.07.028 [PubMed: 28886383]

22. Lee YH, Sharma AR, Jagga S, Lee SS & Nam JS Differential Expression Patterns of Rspondin Family and Leucine-Rich Repeat-Containing G-Protein Coupled Receptors in Chondrocytes and Osteoblasts. Cell J 22, 437–449 (2021). 10.22074/cellj.2021.6927 [PubMed: 32347037]

23. Liu SL et al. LGR6 promotes osteogenesis by activating the Wnt/beta-catenin signaling pathway. Biochem Biophys Res Commun 519, 1–7 (2019). 10.1016/j.bbrc.2019.08.122 [PubMed: 31500806]

24. Doherty L et al. A PDGFRbeta-PI3K signaling axis mediates periosteal cell activation during fracture healing. PLoS One 14, e0223846 (2019). 10.1371/journal.pone.0223846 [PubMed: 31665177]

25. Guntur AR & Rosen CJ The skeleton: a multi-functional complex organ: new insights into osteoblasts and their role in bone formation: the central role of PI3Kinase. J Endocrinol 211, 123–130 (2011). 10.1530/JOE-11-0175 [PubMed: 21673026]

26. Cantley LC The phosphoinositide 3-kinase pathway. Science 296, 1655–1657 (2002). [PubMed: 12040186]

27. Engelman JA, Luo J & Cantley LC The evolution of phosphatidylinositol 3-kinases as regulators of growth and metabolism. Nat Rev Genet 7, 606–619 (2006). 10.1038/nrg1879 [PubMed: 16847462]

28. Adapala NS et al. The loss of Cbl-phosphatidylinositol 3-kinase interaction perturbs RANKL-mediated signaling, inhibiting bone resorption and promoting osteoclast survival. The Journal of biological chemistry 285, 36745–36758 (2010). 10.1074/jbc.M110.12462810.1074/jbc.M110.124628. Epub 2010 Sep 17. [PubMed: 20851882]

29. Adapala NS, Barbe MF, Langdon WY, Tsygankov AY & Sanjay A Cbl-phosphatidylinositol 3 kinase interaction differentially regulates macrophage colony-stimulating factor-mediated osteoclast survival and cytoskeletal reorganization. Annals of the New York Academy of Sciences 1192, 376–384 (2010). 10.1111/j.1749-6632.2009.05346.x [PubMed: 20392263]

30. Adapala NS, Barbe MF, Tsygankov AY, Lorenzo JA & Sanjay A Loss of Cbl-PI3K interaction enhances osteoclast survival due to p21-Ras mediated PI3K activation independent of Cbl-b. Journal of cellular biochemistry 115, 1277–1289 (2014). 10.1002/jcb.24779 [PubMed: 24470255]

31. Adapala NS et al. Loss of Cbl-PI3K interaction in mice prevents significant bone loss following ovariectomy. Bone 67C, 1–9 (2014). 10.1016/j.bone.2014.06.013

32. Buitrago L, Langdon WY, Sanjay A & Kunapuli SP Tyrosine phosphorylated c-Cbl regulates platelet functional responses mediated by outside-in signaling. Blood 118, 5631–5640 (2011). 10.1182/blood-2011-01-328807 [PubMed: 21967979]

33. Adapala NS, Barbe MF Langdon WY. Nakamura MC. Tsygankov AY. Sanjay A. The loss of Cbl-phosphatidylinositol 3-kinase interaction perturbs RANKL-mediated signaling, inhibiting bone resorption and promoting osteoclast survival. The Journal of biological chemistry 285, 36745–36758 (2010). 10.1074/jbc.M110.124628 [PubMed: 20851882]

34. Miyazaki T et al. Src kinase activity is essential for osteoclast function. The Journal of biological chemistry 279, 17660–17666 (2004). 10.1074/jbc.M311032200 [PubMed: 14739300]

35. Molero JC et al. Genetic ablation of the c-Cbl ubiquitin ligase domain results in increased energy expenditure and improved insulin action. Diabetes 55, 3411–3417 (2006). [PubMed: 17130487]

36. Adapala NS, Root S, Lorenzo J, Aguila H & Sanjay A PI3K activation increases SDF-1 production and number of osteoclast precursors, and enhances SDF-1-mediated osteoclast precursor migration. Bone Rep 10, 100203 (2019). 10.1016/j.bonr.2019.100203 [PubMed: 30989092]

37. Scanlon V et al. Loss of Cbl-PI3K interaction modulates the periosteal response to fracture by enhancing osteogenic commitment and differentiation. Bone 95, 124–135 (2017). 10.1016/j.bone.2016.11.020 [PubMed: 27884787]

38. Doherty L a. S., A. LGRs in Skeletal Tissues: An Emerging Role for Wnt-Associated Adult Stem Cell Markers in Bone. JBMR Plus (2020). 10.1002/jbm4.10380

39. Lehoczky JA & Tabin CJ Lgr6 marks nail stem cells and is required for digit tip regeneration Proceedings of the National Academy of Sciences of the United States of America 112, 13249–13254 (2015). 10.1073/pnas.1518874112

40. Ambrosi TH et al. Aged skeletal stem cells generate an inflammatory degenerative niche. Nature 597, 256–262 (2021). 10.1038/s41586-021-03795-7 [PubMed: 34381212]

41. Baron R & Kneissel M WNT signaling in bone homeostasis and disease: from human mutations to treatments. Nat Med 19, 179–192 (2013). 10.1038/nm.3074 [PubMed: 23389618]

42. de Lau W, Peng WC, Gros P & Clevers H The R-spondin/Lgr5/Rnf43 module: regulator of Wnt signal strength. Genes Dev 28, 305–316 (2014). 10.1101/gad.235473.113 [PubMed: 24532711]

43. Knight MN & Hankenson KD R-spondins: novel matricellular regulators of the skeleton. Matrix Biol 37, 157–161 (2014). 10.1016/j.matbio.2014.06.003 [PubMed: 24980904]

44. Bell SM et al. R-spondin 2 is required for normal laryngeal-tracheal, lung and limb morphogenesis. Development 135, 1049–1058 (2008). 10.1242/dev.013359 [PubMed: 18256198]

45. Gong X et al. LGR6 is a high affinity receptor of R-spondins and potentially functions as a tumor suppressor. PLoS One 7, e37137 (2012). 10.1371/journal.pone.0037137 [PubMed: 22615920]

46. Nilsson KH et al. RSPO3 is important for trabecular bone and fracture risk in mice and humans. Nat Commun 12, 4923 (2021). 10.1038/s41467-021-25124-2 [PubMed: 34389713]

47. Zhang M et al. RSPO3-LGR4 Regulates Osteogenic Differentiation Of Human Adipose-Derived Stem Cells Via ERK/FGF Signalling. Scientific Reports 7, 42841 (2017). 10.1038/srep42841 [PubMed: 28220828]

48. Kinzel B et al. Functional roles of Lgr4 and Lgr5 in embryonic gut, kidney and skin development in mice. Dev Biol 390, 181–190 (2014). 10.1016/j.ydbio.2014.03.009 [PubMed: 24680895]

49. Moitra J et al. Life without white fat: a transgenic mouse. Genes Dev 12, 3168–3181 (1998). [PubMed: 9784492]

50. Chan CK et al. Identification and specification of the mouse skeletal stem cell. Cell 160, 285–298 (2015). 10.1016/j.cell.2014.12.002 [PubMed: 25594184]

51. Doherty L, Wan M, Kalajzic I & Sanjay A Diabetes impairs periosteal progenitor regenerative potential. Bone 143, 115764 (2021). 10.1016/j.bone.2020.115764 [PubMed: 33221502]

52. Scanlon V et al. Role of Cbl-PI3K Interaction during Skeletal Remodeling in a Murine Model of Bone Repair. PLoS One 10, e0138194 (2015). 10.1371/journal.pone.0138194 [PubMed: 26393915]

53. Wang X et al. PDGF Modulates BMP2-Induced Osteogenesis in Periosteal Progenitor Cells. JBMR Plus 3, e10127 (2019). 10.1002/jbm4.10127 [PubMed: 31131345]

54. Del Real A et al. Differential analysis of genome-wide methylation and gene expression in mesenchymal stem cells of patients with fractures and osteoarthritis. Epigenetics 12, 113–122 (2017). 10.1080/15592294.2016.1271854 [PubMed: 27982725]

55. Li C et al. Targeted next generation sequencing of nine osteoporosis-related genes in the Wnt signaling pathway among Chinese postmenopausal women. Endocrine 68, 669–678 (2020). 10.1007/s12020-020-02248-x [PubMed: 32147773]

56. Styrkarsdottir U et al. Nonsense mutation in the LGR4 gene is associated with several human diseases and other traits. Nature 497, 517–520 (2013). 10.1038/nature12124 [PubMed: 23644456]

57. Ke J, Ma P, Chen J, Qin J & Qian H LGR6 promotes the progression of gastric cancer through PI3K/AKT/mTOR pathway. Onco Targets Ther 11, 3025–3033 (2018). 10.2147/OTT.S149303 [PubMed: 29872314]

58. Coates BA et al. Transcriptional profiling of intramembranous and endochondral ossification after fracture in mice. Bone 127, 577–591 (2019). 10.1016/j.bone.2019.07.022 [PubMed: 31369916]

59. Chen H et al. PTH 1–34 Ameliorates the Osteopenia and Delayed Healing of Stabilized Tibia Fracture in Mice with Achondroplasia Resulting from Gain-Of-Function Mutation of FGFR3. Int J Biol Sci 13, 1254–1265 (2017). 10.7150/ijbs.21258 [PubMed: 29104492]

60. Zhou X et al. Chondrocytes transdifferentiate into osteoblasts in endochondral bone during development, postnatal growth and fracture healing in mice. PLoS Genet 10, e1004820 (2014). 10.1371/journal.pgen.1004820 [PubMed: 25474590]

61. Julien A et al. FGFR3 in Periosteal Cells Drives Cartilage-to-Bone Transformation in Bone Repair. Stem cell reports 15, 955–967 (2020). 10.1016/j.stemcr.2020.08.005 [PubMed: 32916123]

62. Bahney CS et al. Stem cell-derived endochondral cartilage stimulates bone healing by tissue transformation. J Bone Miner Res 29, 1269–1282 (2014). 10.1002/jbmr.2148 [PubMed: 24259230]

63. Yang G et al. Osteogenic fate of hypertrophic chondrocytes. Cell Res 24, 1266–1269 (2014). 10.1038/cr.2014.111 [PubMed: 25145361]

64. Debnath S et al. Discovery of a periosteal stem cell mediating intramembranous bone formation. Nature (2018). 10.1038/s41586-018-0554-8

65. Bennett CN et al. Regulation of osteoblastogenesis and bone mass by Wnt10b. Proc Natl Acad Sci U S A 102, 3324–3329 (2005). 10.1073/pnas.0408742102 [PubMed: 15728361]

66. Movérare-Skrtic S et al. Osteoblast-derived WNT16 represses osteoclastogenesis and prevents cortical bone fragility fractures. Nature medicine 20, 1279–1288 (2014). 10.1038/nm.3654

67. Ohlsson C et al. Inducible Wnt16 inactivation: WNT16 regulates cortical bone thickness in adult mice. Journal of Endocrinology 237, 113–122 (2018). 10.1530/JOE-18-0020 [PubMed: 29530924]

68. Todd H et al. Wnt16 Is Associated with Age-Related Bone Loss and Estrogen Withdrawal in Murine Bone. PLoS One 10, e0140260 (2015). 10.1371/journal.pone.0140260 [PubMed: 26451596]

69. Movérare-Skrtic S et al. Osteoblast-derived NOTUM reduces cortical bone mass in mice and the NOTUM locus is associated with bone mineral density in humans. Faseb j 33, 11163–11179 (2019). 10.1096/fj.201900707R [PubMed: 31307226]

70. Knight MN et al. R-spondin-2 is a Wnt agonist that regulates osteoblast activity and bone mass. Bone Research 6, 24 (2018). 10.1038/s41413-018-0026-7 [PubMed: 30131881]

71. Luo J et al. LGR4 is a receptor for RANKL and negatively regulates osteoclast differentiation and bone resorption. Nat Med 22, 539–546 (2016). 10.1038/nm.4076 [PubMed: 27064449]

72. Zhu C et al. LGR4 acts as a key receptor for R-spondin 2 to promote osteogenesis through Wnt signaling pathway. Cellular Signalling 28, 989–1000 (2016). 10.1016/j.cellsig.2016.04.010 [PubMed: 27140682]

73. Kato M et al. Cbfa1-independent decrease in osteoblast proliferation, osteopenia, and persistent embryonic eye vascularization in mice deficient in Lrp5, a Wnt coreceptor. J Cell Biol 157, 303–314 (2002). 10.1083/jcb.200201089 [PubMed: 11956231]

74. Kim JA, Choi HK, Kim TM, Leem SH & Oh IH Regulation of mesenchymal stromal cells through fine tuning of canonical Wnt signaling. Stem Cell Res 14, 356–368 (2015). 10.1016/j.scr.2015.02.007 [PubMed: 25863444]

75. Lee H, Seidl C, Sun R, Glinka A & Niehrs C R-spondins are BMP receptor antagonists in Xenopus early embryonic development. Nat Commun 11, 5570 (2020). 10.1038/s41467-020-19373-w [PubMed: 33149137]

76. Zhou YM et al. BMP9 Reduces Bone Loss in Ovariectomized Mice by Dual Regulation of Bone Remodeling. J Bone Miner Res 35, 978–993 (2020). 10.1002/jbmr.3957 [PubMed: 31914211]

77. Huang R, Vi L, Zong X & Baht GS Maresin 1 resolves aged-associated macrophage inflammation to improve bone regeneration. FASEB J 34, 13521–13532 (2020). 10.1096/fj.202001145R [PubMed: 32794246]

78. Chiang N, Libreros S, Norris PC, de la Rosa X & Serhan CN Maresin 1 activates LGR6 receptor promoting phagocyte immunoresolvent functions. J Clin Invest 129, 5294–5311 (2019). 10.1172/JCI129448 [PubMed: 31657786]

79. Im DS Maresin-1 resolution with RORalpha and LGR6. Prog Lipid Res 78, 101034 (2020). 10.1016/j.plipres.2020.101034 [PubMed: 32360520]

80. Arima M et al. R-spondin 2 promotes osteoblastic differentiation of immature human periodontal ligament cells through the Wnt/beta-catenin signaling pathway. J Periodontal Res 54, 143–153 (2019). 10.1111/jre.12611 [PubMed: 30284717]

81. Sharma AR et al. Rspo 1 promotes osteoblast differentiation via Wnt signaling pathway. Indian J Biochem Biophys 50, 19–25 (2013). [PubMed: 23617070]

82. Yu J, Adapala NS, Doherty L & Sanjay A Cbl-PI3K interaction regulates Cathepsin K secretion in osteoclasts. Bone 127, 376–385 (2019). 10.1016/j.bone.2019.07.009 [PubMed: 31299383]

Highlights

- Increased Lgr6 expression in a mouse model with enhanced periosteal response to injury

- The number of Lgr6+ progenitor cells and their progeny are increased on newly formed bone in response bone fracture

- *Lgr6*-null mice have a lower proportion of skeletal stem cells

- *Lgr6*-null mice show deficient proliferation and ALP activity immediately after fracture injury and have impaired endochondral fracture healing
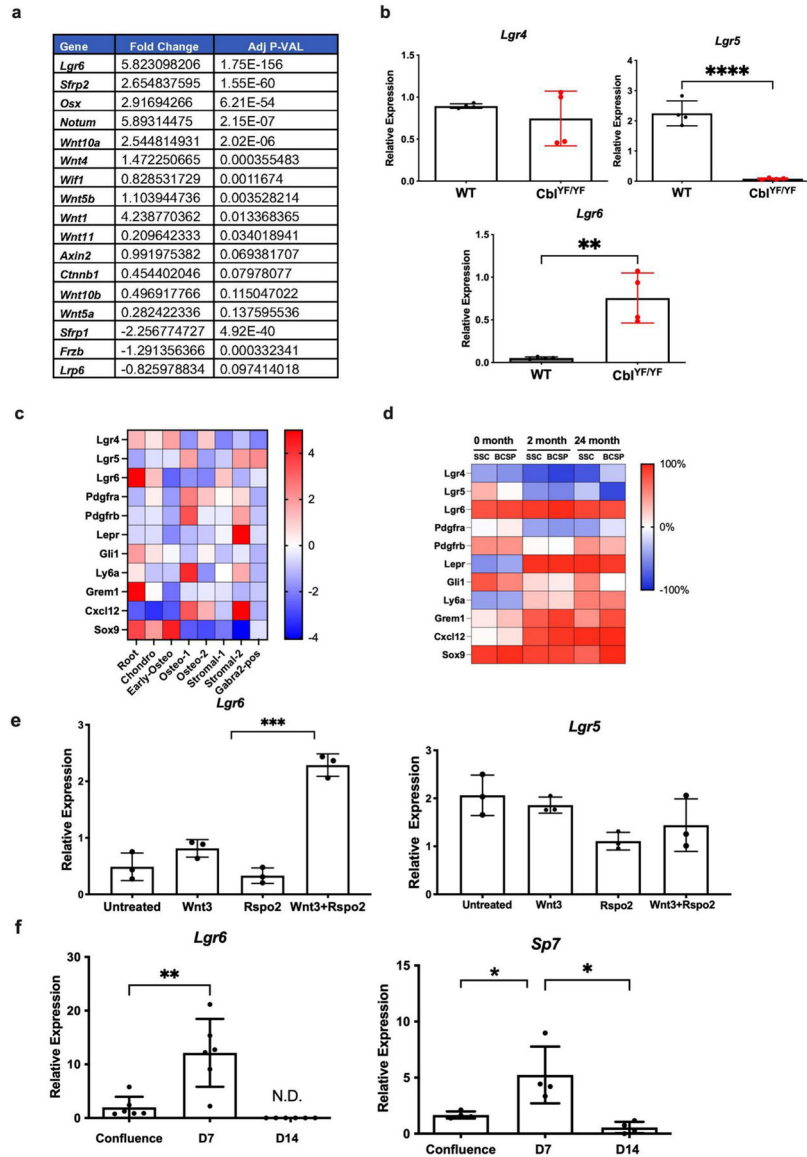
Figure 1.

a. Wnt pathway-related genes identified to be differentially expressed in gCbl^{YF}-derived periosteal cells compared to control. An adjusted *p*-value and log2 fold change value were calculated for each transcript using the publicly available DESeq2 program. **b.** Periosteal cultures were grown to confluence, and the expression of Lgr family members was analyzed by qRTPCR. **c**. To determine Lgr6 expression specifically in skeletal stem cells (SSCs) in bone marrow, we analyzed a recently published annotated scRNA-seq data set of Thy1−CD105−6C3−ITGAV+CD200+ SSCs. The most primitive subgroup of SSC identified was the 'Root' cluster that did not demonstrate a trajectory towards a specific lineage identity; this Root cluster was significantly enriched in *Lgr6* expression. Based on gene enrichment and fate-specification programs, other clusters were annotated as chondrogenic (Chondro), osteogenic(Early-osteo, Osteo-1, Osteo-2), stromal (Stomal-1, Stromal-2), and a GABRA-2+ population, which was under further investigation. **d.** From

the same study, we also analyzed select genes from microarray data from a skeletal stem cell (SSC; CD51$^+$ THY1$^-$6C3$^-$CD105$^-$) and bone-cartilage-stromal progenitor (BCSP; CD51$^+$THY1$^-$6C3$^-$CD105$^+$) population derived from 0–, 2– and 24-month-old mice[33]. Our analysis showed that compared to some of the other SSC markers, Lgr6 expression was minimally changed with aging. **e.** Periosteal cultures were grown to confluence and treated with Wnt3a (50 ng/mL) or a combination of Wnt3a and Rspo2 (50 ng/mL). qRTPCR analysis was performed to detect the expression of *Lgr6 and Lgr5.* **f.** Periosteal cultures were grown to confluence. qRTPCR analysis shows *Lgr6* and *Sp7* expression in isolated periosteal cells is significantly reduced upon 7 days of osteogenic differentiation. n=3 *p<0.05. A representative of 2 experiments is shown.
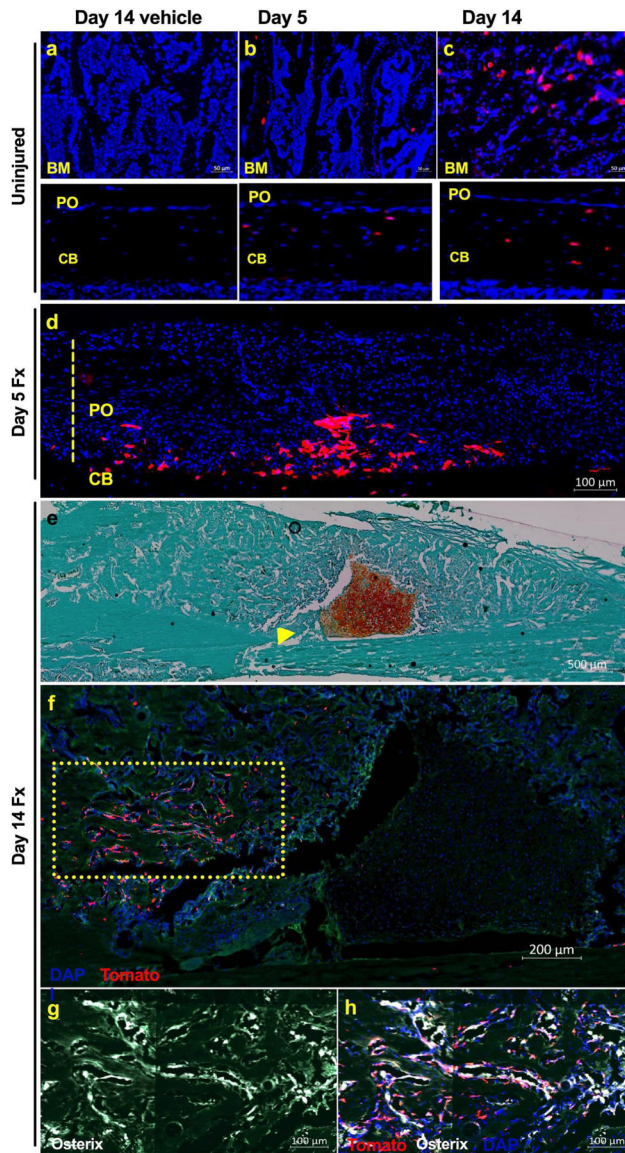
Figure 2.
Lgr6 expression in injured bone. $Lgr6^{EGFP\text{-}ires\text{-}CreERT2}/^{+}$; Ai9/$^{+}$ mice were injected with (a) vehicle or tamoxifen (b-h)) and sacrificed for histological assessment 5- and 14-days after injury. **b-c** . Progeny of Lgr6+ progenitors are labeled tdTomato+ within the non-injured bone marrow, cortical bone. No Tomato+ cells are visible in the periosteum. **d.** Five days post-fracture presence of the progeny of Lgr6+ progenitors labeled tdTomato+ within select areas of the thickened cambium layer. The dotted line shows thickened periosteum. **e.** 14-day post-fracture Safranin O and Fast green staining of sections. Arrow indicates the fracture site. **f.** Progeny of Lgr6+ progenitors labeled tdTomato+ within select area of fracture callus 14-day post fracture. The bone structure is indicated by green autofluorescence, and nuclei are stained with DAPI. The box indicates the magnified area. **g.** Osterix+ immunostaining of bone cells within the callus. **h.** Colocalization of tdTomato+ and osterix+ cells within the

fracture callus. PO=periosteum, CB=cortical bone., BM=bone marrow. 5 days post-fracture. n= 5 mice/condition. Representative images are shown.
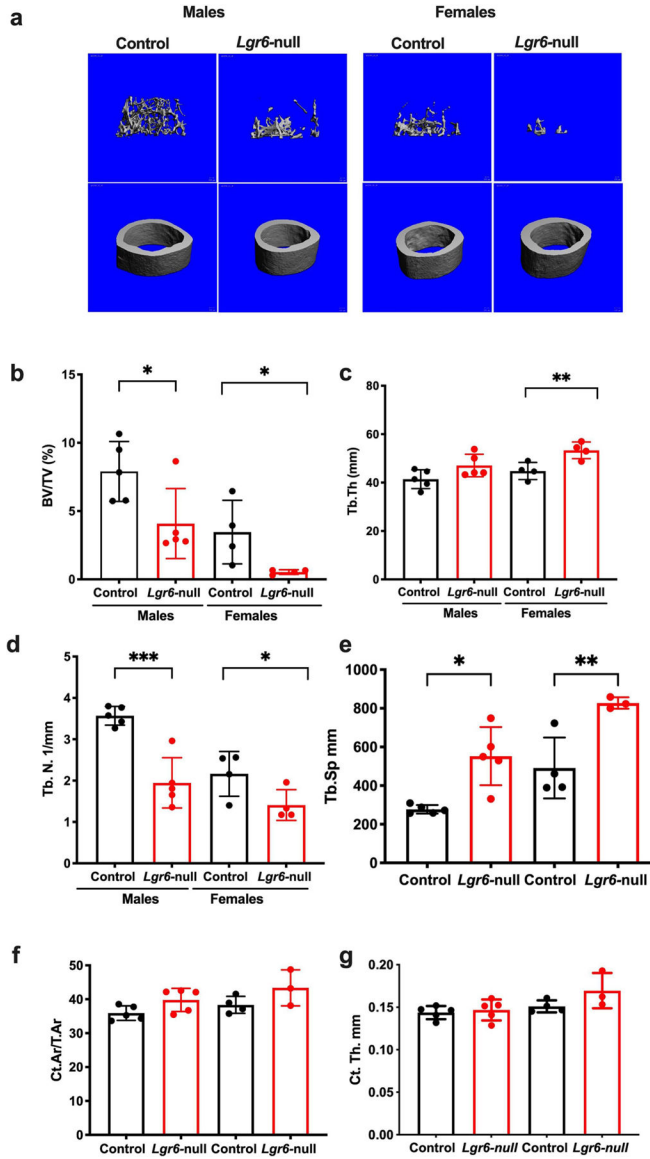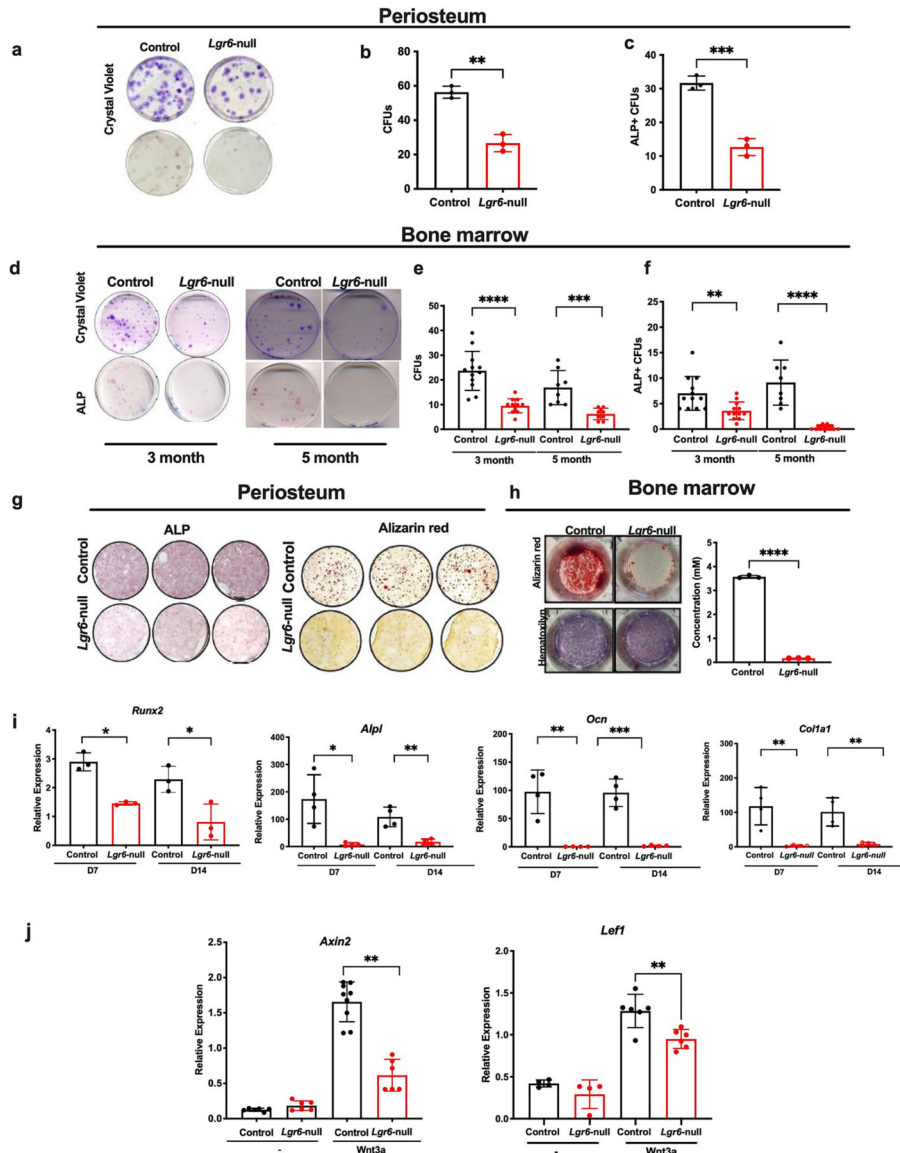
Figure 3.

Lgr6-null mice are osteopenic. **a.** Representative 3D reconstructed μCT images of femoral trabecular bone from 3-and 5-month-old mice from each sex and genotype **b-g.** Quantified trabecular and cortical μCT parameters between genotypes: **b.** bone volume/tissue volume (BV/TV), **c.** trabecular thickness (Tb.Th.), **d.** trabecular number (Tb.N.), **e.** trabecular separation (Tb. Sp), **f.** Cortical area/tissue area (Ct. Ar./T.Ar.) **g.** Cortical thickness (Ct. Th). n= Controls: 5 males and 4 females; *Lgr6*-null: 5 males and 4 females. Quantified bone parameters were analyzed by Student's t-test; sexes were analyzed separately. *p<0.05, **p <0.001, ***p <0.0001 Scale bar 1mm.

Figure 4.

Mesenchymal progenitors isolated from *Lgr6*-null mice have reduced colony-forming potential, reduced osteogenic differentiation capacity, and attenuated response to cWnt signaling. Periosteum (**a-c**) and Bone marrow-derived cells (**d-f**) from *Lgr6*-null and control mice were plated for CFU assays and stained with crystal violet staining to identify colony formation; colonies were stained with alkaline phosphatase to assess osteogenic potential. Colonies were quantified. Mice of both sexes were used. Periosteal cultures are derived from 3-month-old males and females. Cells for each sample were pooled from two individual mice of the same sex. For BMSCs Control, n=8–12 (4–6 males; 4–6 females) *Lgr6*-null, n=9–12 (4–6 males; 5–6 females). Periosteal (**g**) and BMSCs (**h**) from *Lgr6*-null and control mice underwent *in vitro* osteogenesis for 21 days. Periosteal cells were stained for ALP and with alizarin red. BMSCs were stained for alizarin red-S (upper panel), followed by hematoxylin (lower panel). Quantitation of alizarin red-S dye. **i.** qRT-PCR

analyses of osteogenic markers at day 7 and day 14 of osteogenesis of BMSCs. The osteogenic differentiation experiment was performed in triplicates and repeated 3 times. A representative of 3 experiments is shown. **j.** BMSCs grown to confluence were serum starved for 24h and then treated with cWnt3a (100ng/ml) for 6 h. Expression of *Axin2* and *Lef1* was examined. A representative of 2 experiments is shown. Data were analyzed by Students' t-test; *p<0.05, **p <0.01; ***p<0.0001.
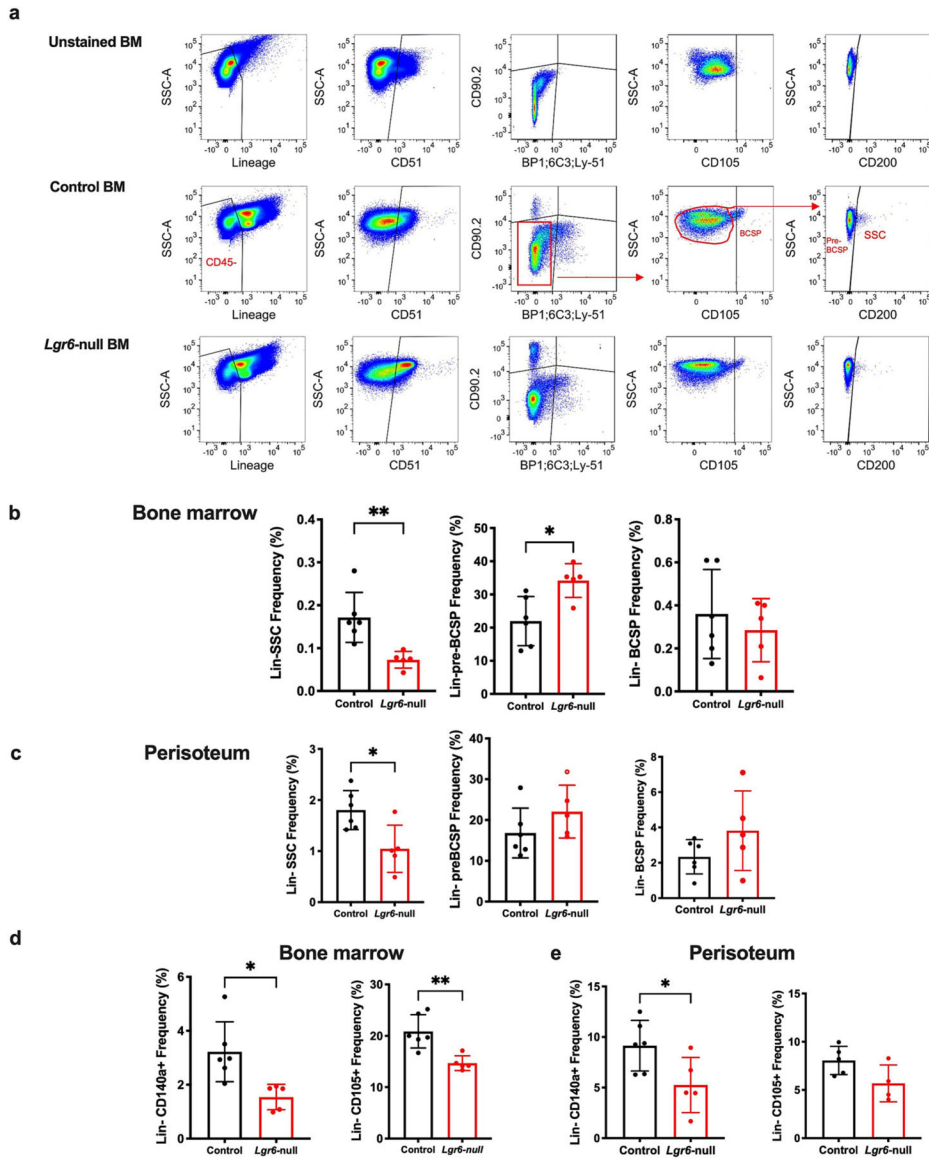
Figure 5.
Bone marrow and periosteal cells derived from *Lgr6*-null mice are composed of a different proportion of skeletal stem cells and progenitors. **a.** Gating strategy to determine proportions of skeletal stem cells and their downstream progenitor in bone marrow from unstained, control, and *Lgr6*-null mice. **b.** Bone marrow analysis of SSCs, pre-BSCPs, and BSCP. Graphs represent one experiment using 5–6 male mice/genotype. **c.** Analysis for SSCs, pre-BSCPs, and BSCP population from periosteum-derived cells. For periosteal samples total of 11–12, male mice from each genotype were used, and cells from 2 mice were pooled for each sample. **d and e.** Cells were also analyzed for a specific population of mesenchymal progenitors, Lin⁻CD140⁺ and Lin⁻CD105⁺, from Bone marrow (d) and periosteum (e). SSC (stem cells), pre-bone cartilage stromal progenitor (pre-BSCP), bone cartilage–stromal progenitor (BSCP). Comparison of control and *Lgr6*-null groups by two-sided Student's t-test adjusted for non-normality (Mann Whitney test) or unequal variance (Welch's test)

where appropriate. All data are mean SD ±, *p<0.05, **p <0.01.A representative of 3 experiments is shown.
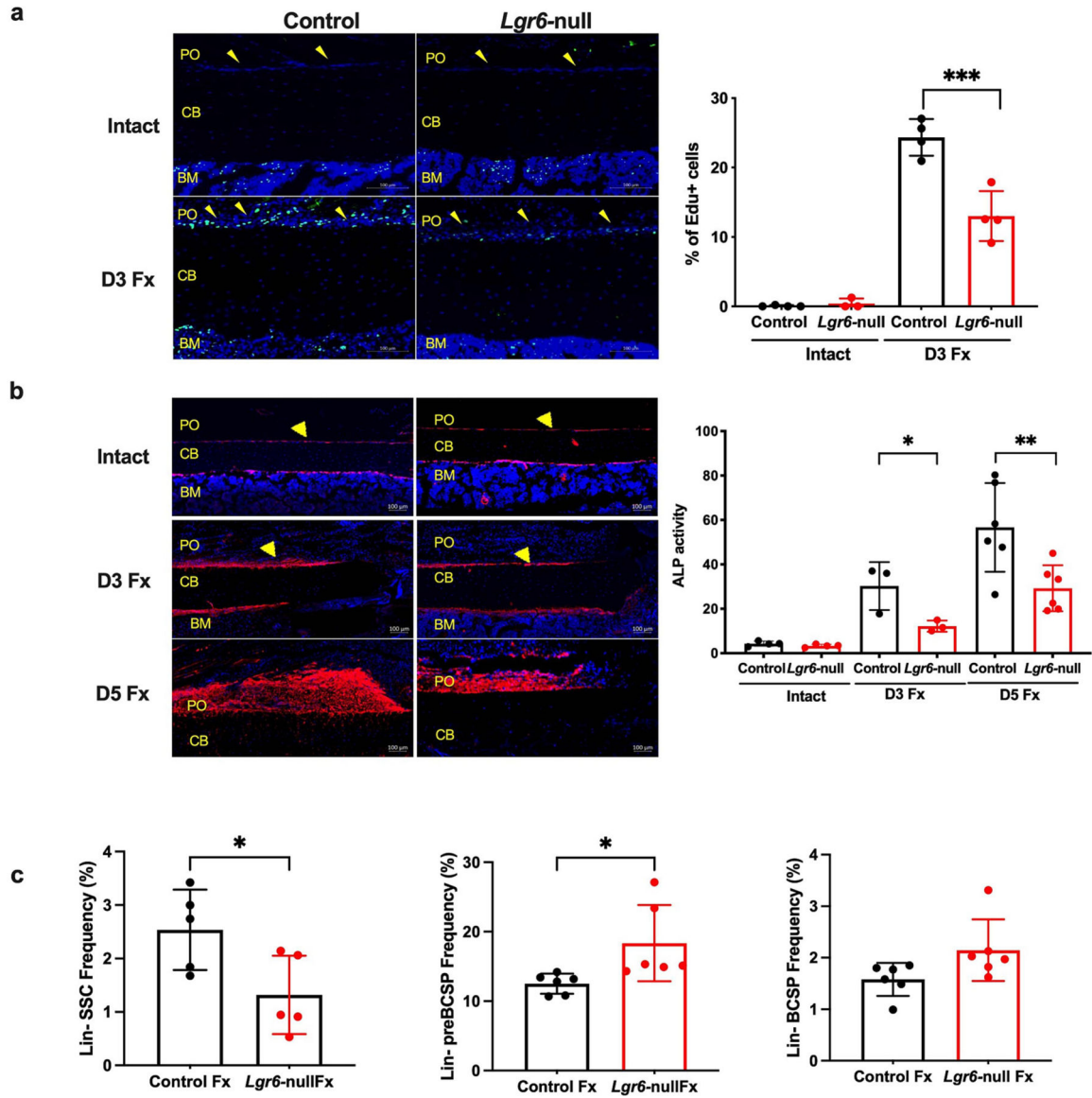
Figure 6.

In response to fracture, *Lgr6*-null periosteum is less proliferative and has decreased ALP activity **a.** 10x images of mid-diaphyseal regions in EdU-labeled and DAPI-stained frozen sections from intact and 3-day fracture femurs from control and *Lgr6*-null mice injected with EdU. Bar graph representing the relative EdU[+] and DAPI^{+} cells within the periosteal region of control and *Lgr6*-null D3 fractured femurs. n=3–4 male mice/genotype. **b.** *Lgr6*-null mice have decreased ALP activity. 10x images of mid-diaphyseal regions in ALP and DAPI-stained frozen sections from intact, 3 -and 5-days post-fracture femurs from control and *Lgr6*-null mice. Bar graph representing the percent ALP[+] periosteal pixels over a fixed threshold of 85 normalized to the total pixels per ROI. n=3–6 male mice/genotype. PO: periosteum, CB: Cortical bone, BM: Bone marrow. **c.** Periosteal cells isolated from the fracture site were analyzed for a population of mouse skeletal stem cells defined as CD90-CD200+ cells from the parent Lin-CD51+Ly51-CD105- population and the downstream

bone, cartilage, and stromal progenitors (BCSPs), defined as CD90-CD105- cells from the parent Lin-CD51+Ly51- population. Cells from 2–3 fractured femurs were pooled, and 11–12 male mice for each genotype were used. A representative of 2experimentst is shown. All data are mean SD ±. *p<0.05, **p <0.01.
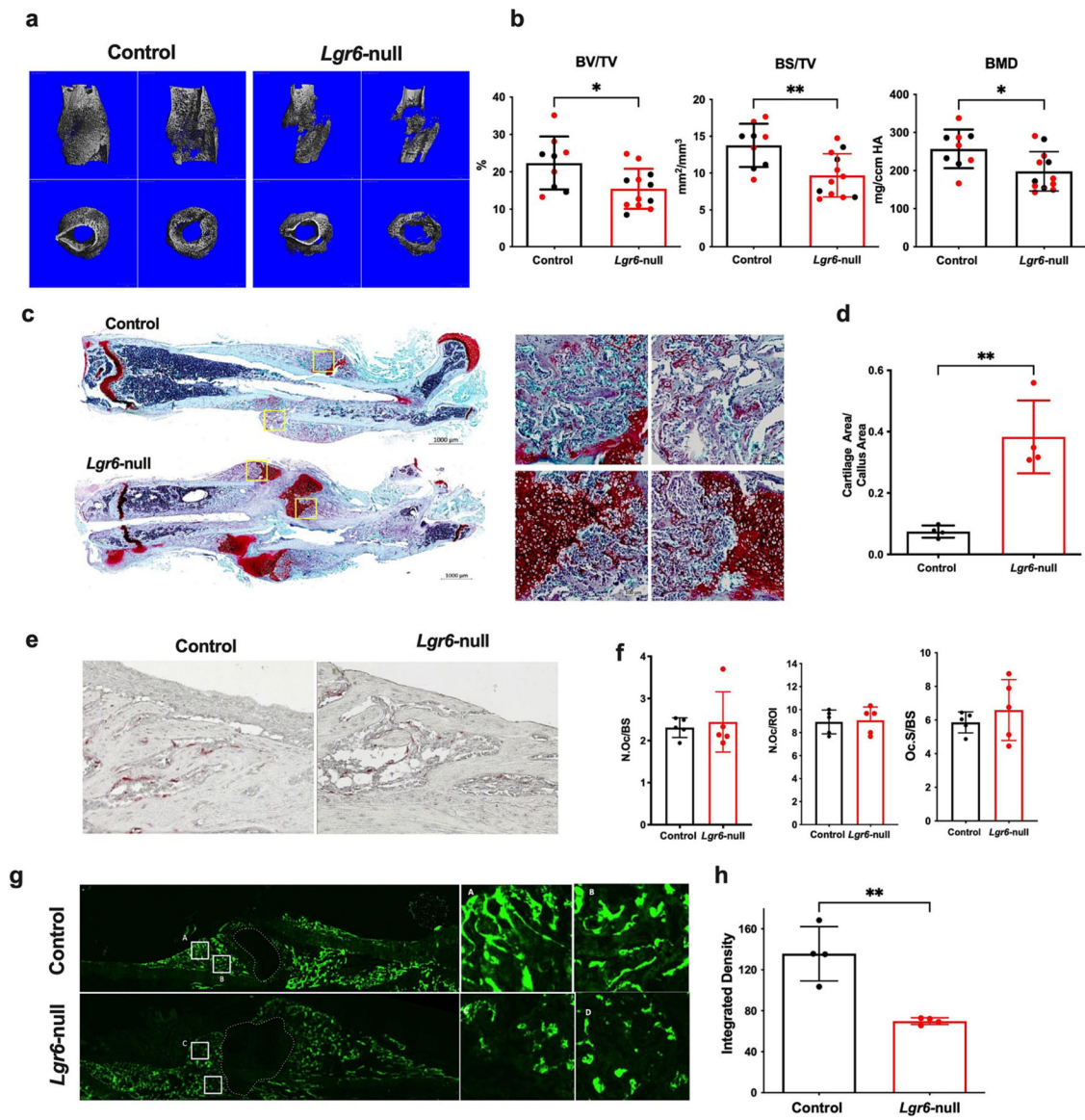
Figure 7.

Lgr6-null mice experience impaired endochondral fracture healing. **a.** Representative 3D μCT images of calluses from fractured femurs 14 days after fracture. **b.** μCT parameters of calluses 14 days post-fracture in control animals compared to *Lgr6*-null. BV/TV=bone volume per total volume within the callus TV=total callus volume. 12-week-old males (red dots) and females (black dots). n=9–12 mice/genotype **c.** Histological section stained with Safranin O/fast green stains of representative fractured bones at day 14 post-fracture. **d.** Quantification of cartilage area in the callus. n=4 mice/genotype. **e.** TRAP staining **f.** quantification of osteoclast parameters from areas flanking the fracture site 14 days post-fracture. n=5 mice/genotype. Scale bar=100μm. N. Oc/ROI=number of osteoclasts in the region of interest, N. Oc/BS=number of osteoclasts per bone surface, Oc. S/BS = osteoclast surface per bone surface. **g.** Calcein was injected one day before sacrifice to label areas of active bone formation in mineralizing areas of the healing fracture. Fluorescent

microscopy images demonstrating the different calcein labeling patterns between and control fracture calluses. **h.** Fluorescence integrated density quantified n=4/male mice/genotype. Scale bar=1000μm.
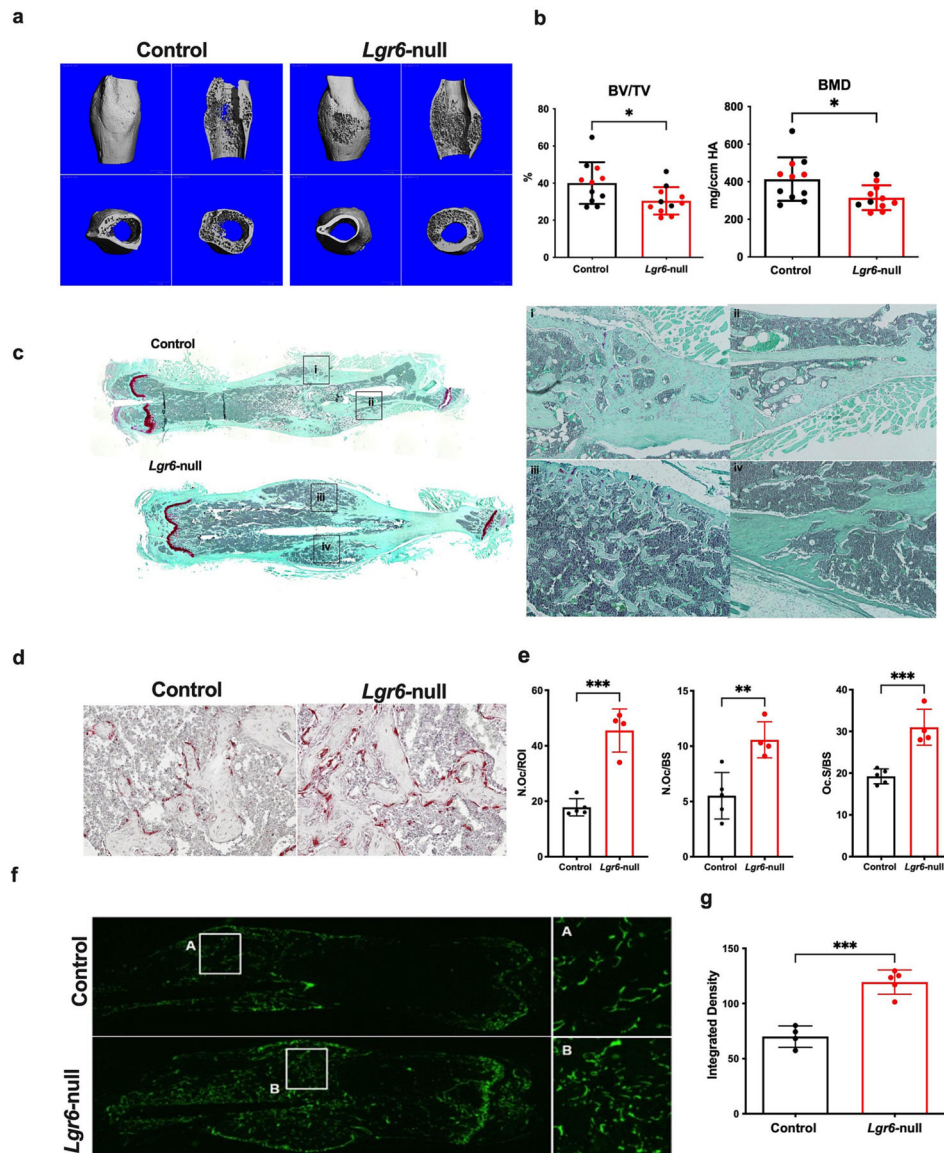
Figure 8.
Post-fracture bone remodeling is delayed in *Lgr6*-null mice. **a.** Representative 3D μCT images of calluses from fractured femurs 28 days after fracture, and **b.** corresponding μCT analysis of fractured bones. 10–12-week-old males/genotype (red dots) and females (black dots). n= 8–11 mice/genotype. **c.** Safranin O/fast green staining of control and *Lgr6-null femurs* 28 days post-fracture. **d.** TRAP staining, **e.** quantification of osteoclast parameters from areas flanking the fracture site 28 days post-fracture. Scale bar=100μm. N. Oc/ROI=number of osteoclasts in the region of interest, N. Oc/BS=number of osteoclasts per bone surface, Oc. S/BS=osteoclast surface per bone surface. **f.** Calcein was injected one day before sacrifice to label areas of active bone formation in mineralizing areas of the healing fracture. Fluorescent microscopy images demonstrating the different calcein

labeling patterns between *Lgr6*-null and control fracture calluses 28 days after fracture. **g.** Fluorescence integrated density quantified n=3–5 male mice/genotype.

Table 1

Femoral microarchitecture assessed by μCT of 5-month-old male and female mice.

	Male		Female	
	Control	**_Lgr6_-null**	**Control**	**_Lgr6_-null**
	Femoral Trabecular Bone			
BV/TV (%)	7.90 ± 2.19	4.08 ± 2.56 [*]	3.46 ± 2.33	0.535 ± 0.167 [*]
BV (mm3)	0.208 ± 0.084	0.105 + 0.080	0.080 ± 0.067	0.0132 ± 0.005
TV (mm3)	2.56 ± 0.381	2.45 ± 0.243	2.41 ± 0.154	2.46 ± 0.110
BS (mm)	12.8 ±3.98	5.63 ± 4.04 [*]	4.67 ± 3.55	0.606 ± 0.242 [*]
BS/BV	65.2 ± 7.04	57.1 ± 3.39	64.8 ± 9.42	48.2 ± 6.59
Trab. Spacing	277 ± 22.0	552 ± 150 [*]	491 ± 158	827 ± 29.8 [**]
Trab. Number	3.57 ± 0.225 [***]	1.95 ± 0.608	2.16 ± 0.541	1.41 ± 0.373 [*]
Trab. Thickness	41.4 ± 3.89	47.1 ± 4.65	44.8 ± 3.52	53.3 ± 3.44 [**]
	Femoral Cortical Bone			
Tt. Ar (mm2)	1.67 ± 0.149	1.37 ± 0.163	1.50 ± 0.111	1.47 ± 0.142
Ct. Ar (mm2)	0.144 ± 0.007	0.147 ± 0.0123	0.151 ± 0.007	0.170 ± 0.020
Ma.Ar mm^2	0.926 ± 0.114	0.739 ± 0.134	0.835 ± 0.0966	0.721 ± 0.152
Ct. Ar/Tt. Ar	35.9 ± 2.15	39.8 ± 3.43	38.4 ± 2.51	43.4 ± 5.31
Ct. Th(mm)	0.144 ± 0.008	0.147 ± 0.012	0.151 ± 0.007	0.170 ± 0.020
Ps. Pm (mm)	4.76 + 0.255	4.51± 0.175	4.53 ± 0.136	4.40 ± 0.212
Ec. Pm (mm)	3.85 ± 0.241	3.32 ± 0.271	3.51 ± 0.170	3.33 ± 0.289
Porosity (%)	0.953 ± 0.051	0.625 ± 0.091 [***]	0.793 ± 0.090	0.572 ± 0.041 [*]

μCT was performed on distal femurs for trabecular bone and the femoral midshaft for cortical bone. Values are means ± SD. *Significantly different compared to controls by one-way ANOVA with Tukey's post-hoc test.

[*] $p < 0.05$

[**] $p < 0.01$

[***] $p < 0.001$